

Room temperature Planar Hall effect in nanostructures of trigonal-PtBi₂

Arthur Veyrat,^{1,2,3,*} Klaus Koepf, ^{1,2} Louis Veyrat,^{1,2,4} Grigory Shipunov,^{1,2}
Iryna Kovalchuk,^{5,1} Saicharan Aswartham,^{1,2} Jiang Qu,^{1,2} Ankit Kumar,^{1,2} Michele
Ceccardi,^{6,7} Federico Caglieris,⁷ Nicolás Pérez Rodríguez,^{1,2} Romain Giraud,^{1,2,8} Bernd
Büchner,^{1,2,9} Jeroen van den Brink,^{1,2,9} Carmine Ortix,^{10,†} and Joseph Dufouleur^{1,2,11,‡}

¹Leibniz Institute for Solid State and Materials Research (IFW Dresden), Helmholtzstraße 20, D-01069 Dresden, Germany

²Würzburg-Dresden Cluster of Excellence *ct.qmat*, Dresden, Germany

³Laboratoire de Physique des Solides (LPS Orsay), 510 Rue André Rivière, 91400 Orsay, France

⁴CNRS, Laboratoire National des Champs Magnétiques Intenses, Université Grenoble-Alpes,
Université Toulouse 3, INSA-Toulouse, EMFL, 31400 Toulouse, France

⁵Kyiv Academic University, 03142 Kyiv, Ukraine

⁶Department of Physics, University of Genoa, 16146 Genoa, Italy

⁷CNR-SPIN Institute, 16152 Genoa, Italy

⁸Université Grenoble Alpes, CNRS, CEA, Grenoble-INP, Spintec, F-38000 Grenoble, France

⁹Department of Physics, TU Dresden, D-01062 Dresden, Germany

¹⁰Dipartimento di Fisica “E. R. Caianiello”, Università di Salerno, IT-84084 Fisciano (SA), Italy

¹¹Center for Transport and Devices, TU Dresden, D-01069 Dresden, Germany

Trigonal-PtBi₂ has recently garnered significant interest as it exhibits unique superconducting topological surface states due to electron pairing on Fermi arcs connecting bulk Weyl nodes. Furthermore, topological nodal lines have been predicted in trigonal-PtBi₂, and their signature was measured in magnetotransport as a dissipationless, *i.e.* odd under a magnetic field reversal, anomalous planar Hall effect. Understanding the topological superconducting surface state in trigonal-PtBi₂ requires unravelling the intrinsic geometric properties of the normal state electronic wavefunctions and further studies of their hallmarks in charge transport characteristics are needed. In this work, we reveal the presence of a strong dissipative, *i.e.* even under a magnetic field reversal, planar Hall effect in PtBi₂ at low magnetic fields and up to room temperature. This robust response can be attributed to the presence of Weyl nodes close to the Fermi energy. While this effect generally follows the theoretical prediction for a planar Hall effect in a Weyl semi-metal, we show that it deviates from theoretical expectations at both low fields and high temperatures. We also discuss the origin of the PHE in our material, and the contributions of both the topological features in PtBi₂ and its possible trivial origin. Our results strengthen the topological nature of PtBi₂ and the strong influence of quantum geometric effects on the electronic transport properties of the low energy normal state.

INTRODUCTION

Topology is, together with superconductivity, one of the most striking macroscopic manifestation of the quan-

tum nature of electrons in quantum materials. A consequence of the geometric properties of the wave function, from which topological properties arise, is the existence of the Berry curvature (BC): an emerging magnetic field in momentum space. In a Weyl semi-metal, the Weyl nodes act as sources and sinks of BC [1] and can lead to signatures in charge-transport experiments such as the planar Hall effect (PHE) [2–4]: the appearance under an external in-plane magnetic field of a transverse voltage dependent on the relative orientations of the current and magnetic field. The PHE is dissipative, *i.e.* it is symmetric in magnetic field and associated with an in-plane field-dependent longitudinal voltage called anisotropic magnetoresistance (AMR) [5]. However, mechanisms different from the BC such as intrinsic or orbital magnetism can also result in a dissipative PHE and AMR, making it an ambiguous signature of quantum geometric properties [6, 7].

Here, we study the PHE in magnetic field and temperature to find new insight on the quantum geometric properties in trigonal-PtBi₂: a non-magnetic Weyl- and nodal-line-metal which was recently reported in transport experiments to exhibit sub-Kelvin 2D-superconductivity and a BKT transition in nanostructures [8]. Scanning tunnelling spectroscopy (STS) studies in this compound have reported higher-temperature surface superconductivity [9], which was confirmed by angle-resolved photoemission spectroscopy (ARPES) to be intrinsically – and solely – generated by topological Fermi arcs [10] (The presence of Fermi arcs was also confirmed by STS measurements [11]). Cuts of the DFT calculated band structure through Weyl nodes, as well as the position of the nodes in the Brillouin zone, can be seen in Figure 1. This makes t-PtBi₂ a very promising candidate for intrinsic topological superconductivity.

A thorough investigation of the transport signatures of topological degeneracies in t-PtBi₂ are however still

lacking. Here, we focus on the bulk properties of t-PtBi₂ nanostructures and report on a robust dissipative PHE from low magnetic fields and up to room temperature. These results are entirely coherent with the predicted Weyl nature of t-PtBi₂. We note that, in a complementary study based on the same raw data[12], we evidence and thoroughly analysed another effect known as the anomalous PHE (APHE). This effect, which is two orders of magnitude weaker PHE than the PHE, does not originate from Weyl nodes already existing without external magnetic field, but rather from a conversion of topological nodal lines (which we also predict in that separate study) into very distant Weyl nodes (in k-space). Because of their different origin and different analysis required for both signals, as well as the fact the APHE constitutes but a small perturbation compared to the PHE signal, the two effects are studied separately in each study and the latter is simply ignored in the present study.

PLANAR HALL EFFECT

Planar Hall effect in Weyl Semi-metals

The planar Hall effect is a generic signature of the anisotropy of the magnetoresistivity that uniquely depends on the relative orientations of the in-plane magnetic field and electric field (i.e. current) in the sample. It thus corresponds to a difference $\Delta\sigma = \sigma_{\parallel} - \sigma_{\perp}$ between the conductivity σ_{\parallel} when the two fields are aligned, and the conductivity σ_{\perp} when they are orthogonal. As a result, it manifests itself both in transverse and longitudinal resistance measurements (the latter being sometimes referred to as anisotropic magnetoresistance, AMR, or anisotropic longitudinal magnetoconductance, LMC). Since the two effects (PHE and LMC/AMR) are in a one-to-one correspondence linked, we will refer to them both as PHE from here on. The planar Hall effect has historically been predicted and discovered in ferromagnets [13, 14], where the anisotropy is caused by the concomitant presence of intrinsic magnetization of the material and spin-orbit interaction. In materials without long-range magnetic order, a giant PHE has been predicted to occur in Dirac and Weyl semi-metals as a direct consequence of the chiral anomaly [2, 3]. This results in a large negative contribution to the longitudinal magnetoresistance when the magnetic and electric fields are aligned [2, 15]. In the simple case of a type-I Weyl cone (i.e. when the Weyl cone is not tilted), the contributions of the PHE to the longitudinal conductivity σ_{xx} and the transverse conductivity σ_{yx} follow the angular dependence [3]:

$$\begin{aligned}\sigma_{xx}^{PHE}(\varphi) &= \sigma_{\perp} + \Delta\sigma \cos^2 \varphi, \\ \sigma_{yx}^{PHE}(\varphi) &= \Delta\sigma \sin \varphi \cos \varphi,\end{aligned}\quad (1)$$

with $\Delta\sigma = \sigma_{\parallel} - \sigma_{\perp}$; $\sigma_{\perp} = \sigma_D$ the Drude conductivity, independent of the magnetic field ; $\sigma_{\parallel} = \sigma_D + a \times B^2$ with a a constant which depends on the carrier group velocities and the BC, and B the amplitude of the in-plane magnetic field ; and φ the relative angle between the magnetic and electric fields in the sample. As can be seen from Equation 1, the PHE is characterized by a π -periodic oscillation of both the longitudinal and transverse conductivities, when the magnetic field is rotated in-plane (while keeping the current direction fixed), with a $\pi/4$ offset between them, and the amplitude of the oscillations is expected to increase quadratically with magnetic field.

When the Weyl cones (WC) acquire a tilt (or an overtilt in the case of type-II Weyl cones), the field dependence of the PHE depends on the orientation of the current: when the current flows along the tilt direction, the amplitude of the PHE is expected to grow linearly for small magnetic fields. When the current flows perpendicular to the tilt direction however, the PHE is expected to grow quadratically with field, precisely as for non-tilted Weyl cones [3]. In real materials, the tilt vector can be pinned to principal crystallographic directions by multiple point-group symmetries (e.g. mirror symmetries). However, in materials with low-symmetry content the tilt vector will not be aligned with the crystallographic axes.

We note that, despite its historical name, the planar Hall effect is mostly a magnetism or band structure effect, and isn't typically linked to any Lorentz force from the (in-plane) magnetic field acting on the charge carriers.

Resistivity versus conductivity

We first recall that in magnetotransport experiments, we have no direct access to the conductivity. Instead, we measure the resistance of the sample, which is linked to the resistivity through the geometry of the sample. The behaviour of the resistivity contribution of the PHE is actually expected (in the type-I case at least) to follow very closely that of the conductivity [2, 6]:

$$\begin{aligned}\rho_{xx}^{PHE}(\varphi) &= \rho_{\perp} - \Delta\rho \cos^2 \varphi, \\ \rho_{yx}^{PHE}(\varphi) &= -\Delta\rho \sin \varphi \cos \varphi,\end{aligned}\quad (2)$$

with $\Delta\rho = \rho_{\perp} - \rho_{\parallel}$ the amplitude of the PHE ; $\rho_{\perp} = 1/\sigma_D$ constant in magnetic field ; and $\Delta\rho \propto B^2$ (in the type-I case). Note that the sign convention for $\Delta\rho$ from Ref. [2] is opposite that of $\Delta\sigma$ from Ref.[3].

While Equation 2 is the equation generally adopted in the community, we note that it is only valid in the absence of anisotropies in the zero-field conductivity matrix, i.e. when the Drude conductivity doesn't depend on the direction of the current ($\sigma_D(I_x) = \sigma_D(I_y)$). Even

in the absence of anisotropies, the quadratic field dependence of $\Delta\rho$ is only correct in the small oscillations limit, i.e. when $r = \Delta\sigma/\sigma_D \ll 1$. As this ratio increases (i.e. as the field increases), the field dependence of $\Delta\rho$ slows down, and it ultimately saturates at high field, with

$$\lim_{r \rightarrow \infty} \Delta\rho(r) = 1/\sigma_D.$$

Together with the mixed linear and quadratic field dependence terms expected in the case of tilted WCs, this may explain why most experimental papers studying the PHE in topological semi-metals have reported sub-quadratic field dependences [4, 16–18]. The expected angular dependence of the resistance is represented in Figure 2.a, with R_{xx} in blue and R_{yx} in red. The longitudinal resistance R_{xx} is maximal when magnetic field and current are aligned, while the transverse resistance R_{yx} vanishes in this configuration.

Planar Hall effect in nanostructures of t-PtBi₂

We studied the planar Hall effect in three exfoliated nanostructures of PtBi₂, contacted by standard e-beam lithography techniques. The samples used in this study are denoted as *D1* (70 nm thick), *D2* (126 nm thick) and *D4* (41 nm thick), and their measurement configurations are shown in Figure 3. More details about the structures can be found in the methods section. In previous studies, the two-dimensional superconductivity of these samples was studied in details at sub-Kelvin temperatures [8], and an anomalous planar Hall effect was reported for *D1* and *D2* [12]. Here, we focus on measurements performed from room temperature down to 1 K, above the superconducting transition. No evidence of aging effects was observed between our studies, as indicated by the absence of any measurable change in the residual resistance ratio ($RRR = R(300K)/R(4K)$, see supplementary information Ref. [12]).

The PHE in PtBi₂ was measured first in 2-dimensional in-plane magnetic field mappings of the longitudinal and transverse resistance at 1 K with a 3D vector magnet (Figure 3). The resistance was measured using external lock-in amplifiers, with an AC current of 20 μ A at a frequency of 113 Hz, with an integration time of 300 ms. Although the magnetic field range is limited to 1.5 T in either in-plane directions in this setup, the AMR and PHE are clearly visible in the mappings, through their π -periodicity and $\pi/4$ rotation between longitudinal and transverse measurements. The features at low field in Figure 3.g,h are associated with remnants of the superconductivity in the sample. We extract from the mappings the angular dependence of the resistance at fixed fields B_0 , between 500 mT and 1.5 T. In order to have enough data points for analysis, we consider all points within 20 mT of B_0 (i.e. we extract all points with $|B - B_0| < 20$ mT).

The angular dependence obtained at 1.5 T and 1 K is shown for all three samples in Figure 3.j,k,l, and displays the features expected for the PHE for both longitudinal (R_{xx} , top panels) and transverse (R_{yx} , bottom panels) resistances. The maxima of longitudinal resistance correlate well with the expected orientation of the current in the samples. The data also shows some visible 2π -periodic signal, which may come from stray out-of-plane-field magnetoresistance (MR) due to a misalignment between the samples' planes and the magnetic field plane. We can fit the data very well using a constrained PHE model based on Equation 2, which takes into account a 2π -periodic contribution (more details on this model in the next sections, see Equation 4).

Field and temperature dependences of the PHE

To study the PHE in more details, we measured samples *D1* and *D2* in a Dynacool 14T PPMS using an insert equipped with a mechanical 2D rotator. By rotating the sample with the rotator, the angle φ between the fixed-axis magnetic field and the applied current can be adjusted over a full range of 360° . The resistance was measured using external lock-in amplifiers, with an AC current of 100 μ A at a frequency of 927.7 Hz, with an integration time of 300 ms. In the main text, we will focus on results obtained for sample *D1*, although the same analysis was done for sample *D2*, with similar conclusions (see Supplementary Materials).

For measurements done at $T = 5$ K and $B = 1, 2, 3, 4, 5, 6, 7, 10$ T, as well as at $B = 14$ T and $T = 5, 10, 20, 50, 300$ K, 10 points were measured in succession at each angular position, and their resistance was averaged. The angular step for each measurement was 1° . More precise measurements were taken at $B = 14$ T and $T = 5, 100, 200$ K, with 40 points measured in succession at each angular position, and their resistance averaged. The angular step for each measurement was 0.5° , and the results were interpolated with a step of 1° , to perform the analysis in the same way for each pair of (B,T) parameters.

The measurements done at $T = 5$ K and $B = 14$ T are presented in Figure 4.a, and show a large π -periodic oscillation corresponding to the PHE. Again, the phase of the oscillations correlates well with the expected orientation of the current in the sample. The PHE is already visible at 1 T, the lowest magnetic fields measured (see Figure 5.a), and its magnitude increases with the magnetic field, with a power law that remains in very good agreements with the low field data (see Supplementary Materials). The amplitude of the PHE decreases with increasing temperature (Figure 5.b), and the PHE is very robust with temperature, and can be observed at 14 T up to room temperatures, as shown in Figure 4.c.

Analysis of the results

Beyond the π -periodicity and $\pi/4$ offset between the longitudinal and transverse oscillations, and the correlation between the orientation of the current and the phase of the oscillations, an important characteristic of the PHE is the expected equal amplitude of both oscillations in resistivity (see Equation 2). A more complex analysis is required to confirm this point in real systems, as measurements can only access the resistance, and not the resistivity. In the ideal case, the conversion between the two follows the formulae:

$$\begin{aligned} R_{xx} &= \frac{L}{W \times t} \cdot \rho_{xx} = \frac{N_{\square}}{t} \cdot \rho_{xx}, \\ R_{yx} &= \frac{1}{t} \cdot \rho_{yx}, \end{aligned} \quad (3)$$

with L the distance between the longitudinal contacts, W the width of the sample, t its thickness, and $N_{\square} = L/W$ the number of squares between the longitudinal contacts. In this paper, and unless stated otherwise, we do not consider the thickness of the sample in this calculation (i.e. we take $t = 1$) as it doesn't change the relative amplitudes between R_{xx} and R_{yx} .

A careful analysis of the measurements is necessary, as we need to take into consideration the contributions of several additional signals, coming from different origins. First, as the shape of the samples deviates from the traditional Hall-bar, geometrically estimating accurately N_{\square} between a pair of contacts is not trivial. This is further complicated by the position of the contacts on top of the flake, going inwards. It has been shown that such intrusive contacts can distort current flow and significantly reduce the measured amplitude of the transverse signal (possibly by as much as 50-75% in geometries similar to ours) [19]. We therefore consider an arbitrary reduction in the amplitude of the transverse resistance measured compared to its full amplitude.

Second, if the transverse contacts are not perfectly aligned orthogonally to the direction of the current, the resistance measured between them will include a longitudinal contribution, which can be significant as the longitudinal and transverse signals in the PHE have the same amplitude. In a traditional Hall configuration, such extra contributions due to contact misalignment can be removed by symmetrising (resp. asymmetrising) the longitudinal (resp. transverse) resistance in magnetic field, as the longitudinal and Hall signals are expected to be respectively even and odd in field. However in our system and configuration, such a procedure cannot be applied, such that we must consider an additional longitudinal contribution to the transverse resistance, with an arbitrary amplitude, in the fit.

Finally, as mentioned above, we must consider that the sample may not lie exactly in the rotation plane. When

a magnetic field is applied in the rotation plane, this will result in a component of the magnetic field being perpendicular to the sample's plane, and thus in a regular magnetoresistance component in both longitudinal and transverse resistances. As the sample is rotated, the amplitude of the out-of-plane field will vary 2π -periodically, resulting in additional magnetoresistance contributions to the longitudinal and transverse resistances (with π - and 2π -periodicity, respectively). In order to account for any possible 2π -periodic background, we consider additional 2π -periodic signals in both resistances ($R_{xx}^{2\pi}$ and $R_{yx}^{2\pi}$). Any out-of-plane field component should therefore result in a deviation of the longitudinal resistance from our fit, as discussed in the next section.

When all these contributions are considered, our system can be described with

$$\begin{aligned} R_{xx}(B, \varphi) &= R_{xx}^{2\pi}(B, \varphi) + N_{\square} \cdot \rho_{xx}^{\text{PHE}}(B, \varphi), \\ R_{yx}(B, \varphi) &= R_{yx}^{2\pi}(B, \varphi) + C_T \cdot \rho_{yx}^{\text{PHE}}(B, \varphi) + C_L \cdot R_{xx}(B, \varphi), \end{aligned} \quad (4)$$

with

$$\begin{aligned} \rho_{xx}^{\text{PHE}}(\varphi) &= \rho_{\perp} - \Delta\rho \cos^2 \varphi, \\ \rho_{yx}^{\text{PHE}}(\varphi) &= -\Delta\rho \cos \varphi \sin \varphi, \\ R_{xx}^{2\pi}(B, \varphi) &= A_{xx}(B) \cos(\varphi - \varphi_L), \\ R_{yx}^{2\pi}(B, \varphi) &= A_{yx}(B) \cos(\varphi - \varphi_T) + C. \end{aligned} \quad (5)$$

Here, $\Delta\rho = \rho_{\parallel} - \rho_{\perp}$ is the amplitude of the PHE ; $\varphi = \tilde{\varphi} - \varphi_{\text{PHE}}$ is the angle between the magnetic field and the current in the sample, with $\tilde{\varphi}$ the angular position of the sample set by the rotator and φ_{PHE} the rotator angle for which current and field are aligned ; $R_{xx}^{2\pi}$ and $R_{yx}^{2\pi}$ are 2π -periodic background contributions with arbitrary angular origins φ_L and φ_T ; C is a field-independent offset of the transverse resistance ; and N_{\square} , C_T and C_L are respectively the effective number of squares between longitudinal contacts, the correcting factor for the transverse resistance due to the invasive contacts, and the correcting factor due to the misalignment of the contacts. The same analysis is performed in temperature, with the addition of a temperature-dependent vertical offset to the background terms to account for the resistance increasing with temperature:

$$\begin{aligned} R_{xx}^{2\pi}(T, \varphi) &= A_{xx}(T) \cos(\varphi - \varphi_L) + C_{xx}(T), \\ R_{yx}^{2\pi}(T, \varphi) &= A_{yx}(T) \cos(\varphi - \varphi_T) + C_{yx}(T). \end{aligned} \quad (6)$$

Due to the large number of unknown parameters, it is not possible to get meaningful values for the different variables by fitting a single set of angular dependence (i.e. $R_{xx}(B_0, \varphi)$ and $R_{yx}(B_0, \varphi)$) with Equation 4. We can however overcome this issue by noting that most of these parameters are geometric and therefore independent of the external magnetic field. Thus, by fitting $R_{xx}(B, \varphi)$ and $R_{yx}(B, \varphi)$ together at multiple fields B , and fixing

the geometric parameters as global parameters across all fits, we can extract meaningful values for each parameter, and recover the amplitude of the PHE in resistivity.

The results obtained are shown as thick lines in Figure 4, and present an excellent agreement with the experimental data for both samples, with only small deviations from the model at low fields and high temperatures, which we will discuss shortly (see Figure 6). The dependence of the PHE amplitude $\Delta\rho$ with field and temperature is shown in Figure 5. $\Delta\rho$ increases with field, following the power laws $\Delta\rho \propto B^{1.24}$, which is consistent with low field measurements (see Supplementary materials), and is notably lower than the expected quadratic behavior expected for the pure chiral anomaly effect [2].

As mentioned before, both BC effects and orbital magnetic moment effects could contribute to this sub-quadratic field dependence [20]. Importantly, $\Delta\rho$ starts decreasing with temperature above $T \sim 20$ K, and remains clearly visible up to room temperature, with $\Delta\rho \simeq 0.34 \mu\Omega\cdot\text{cm}$, which is relatively large for a non-magnetic system.

DEVIATIONS FROM PHE MODEL

As stated above, and as can be seen in Figure 4.c, the constrained model of Equation 4 deviates from the data towards low magnetic fields and high temperatures. In the following, we will detail and analyse these deviations and provide possible explanations.

Planar Hall effect at low field and at high temperature

At low temperature $T = 5$ K and low magnetic fields $B \leq 3$ T, while the oscillations from the PHE are still clearly visible in both samples (see Figure 6.a,b,c), the constrained model (thick lines) deviates significantly from the data, due mainly to a phase offset of the oscillations as well as a vertical offset. The amplitude of the oscillations is however well represented by the model. Both offsets decrease quickly with field. At high field ($B = 14$ T) and high temperature $T \geq 100$ K on the other hand, there are no vertical or phase offsets between the constrained model and the data. However, while the model still fits closely the data in R_{yx} , it starts deviating at high temperatures from the data in R_{xx} , as shown in Figure 6.e,f,g (thick lines). This is due to both oscillations no longer sharing the same amplitude, which is incompatible with the PHE model. In order for the fit to keep converging meaningfully at high temperature, we chose to artificially give a higher weight to the data in R_{yx} than in R_{xx} , which is why the deviations is seen only in R_{xx} .

Simple model

While the data deviates from the constrained model of Equation 4, we note that the general shape of the data can still accurately be described by π -periodic oscillations. Thus, to study the deviations from the constrained model in more details, we fitted the data for R_{xx} and R_{yx} independently with an unconstrained model, which includes only two contributions: π -periodic, and 2π -periodic:

$$R(\varphi) = C + A^{2\pi} \cdot \cos(\varphi - \varphi_{2\pi}) + A^\pi \cdot \cos[2(\varphi - \varphi_\pi)], \quad (7)$$

with C an angle-independent constant, and A^π and $A^{2\pi}$ the amplitudes of the π - and 2π -periodic signals, with angular origins φ_π and $\varphi_{2\pi}$, respectively. The results are shown in Figure 6 in dashed lines, and fit the data closely at all fields and temperatures.

The phase and amplitude of the π -periodic oscillations in R_{xx} and R_{yx} can be extracted from this model, and the field and temperature dependence are shown in Figure 6.d,h. For comparison, we show the amplitudes reduced by their values at $B = 14$ T, $T = 5$ K. We also subtract 45° from the phase in R_{yx} , to account for the expected $\pi/4$ shift between R_{yx} and R_{xx} . As expected, the amplitudes of the oscillations in R_{xx} and R_{yx} have the same field dependence at low temperature, in both samples (see Figure 6.d, top panel). The phase of the oscillations, however, shows a strong variation at low magnetic field (Figure 6.d, bottom panel). While the phase of the oscillations in R_{yx} stabilizes quickly, at about 2 T, it continues increasing slowly in R_{xx} over the full angular range. The difference in phase for both oscillations eventually come within a few degrees of the expected $\pi/4$ at higher field, without reaching that value. The other sample, *D2*, shows slightly different features (see Supplementary materials), with only a small variability of the phase at low field, which might be attributed to a lower signal-to-noise ratio. The shift between the oscillations in R_{xx} and R_{yx} deviates from the expected value of 45° by about 5° , which remains about constant over the entire magnetic field range. The variability of the phase in *D1* might be related to current jetting in the sample, which does not have a standard Hall bar shape: If the current lines change orientation as the magnetic field is increased, e.g. to minimize the magnetoresistance, this could lead to a change in the phase of the PHE, which depends on the relative orientation of the magnetic field and the current. As *D2* is closer to the Hall bar shape, the effect of current jetting would be expected to be lower, and the phase variation in field attenuated as well. The deviation from the $\pi/4$ offset between R_{xx} and R_{yx} might also be related to the shape of the samples: As neither *D1* nor *D2* are perfect Hall bars, the resistance between the transverse contacts will also include a longitudinal

contribution. Since $a \cdot \cos \phi + b \cdot \sin \phi = R \cdot \cos(\phi - \alpha)$, with $R = \sqrt{a^2 + b^2}$ and $\alpha = \tan^{-1}(b/a)$, the longitudinal contribution is equivalent to a renormalization and phase offsetting of the transverse signal.

The same analysis is performed at $B = 14$ T and temperatures ranging from $T = 5$ K to $T = 300$ K, and the results are shown in Figure 6.h. As expected, no large variation is observed in the phase of the oscillations, with a few degrees separating the phase in R_{xx} and R_{yx} , as before. However, the temperature dependence of the amplitude of the oscillations is now different between the two resistances, with the amplitude in R_{xx} decreasing more slowly than in R_{yx} . This effect is clearly visible in both samples (see Supplementary materials for *D2*), and is the reason for the deviation between the constrained model and the data.

There are, broadly, two mechanisms which could cause this discrepancy between R_{xx} and R_{yx} . The first mechanism relates to the geometry of the sample and the flow of current. In our analysis, we have considered these parameters (i.e. N_{\square} , C_T , C_L etc.) as independent of magnetic field and temperature. As these parameters relate the resistance to the resistivity, they provide us directly with the link between the amplitude of the oscillations between R_{xx} and R_{yx} . However, if (some of) these parameters were to vary with temperature, this would change the expected balance between the two amplitudes, and may cause the observed discrepancy. Although the exact geometry of the current flow may vary slightly with temperature due to inhomogeneities in the sample, for instance around the invasive contacts, leading to slightly different temperature dependence of the resistance, we cannot think of an effect strong enough to cause the observed difference in amplitude. The second mechanism would be the existence of a second π -periodic effect in R_{xx} , distinct from the PHE. This effect would need to have a small amplitude at low temperature with respect to the PHE, as the latter accounts well for the data at low temperature. If such an effect did exist, and its amplitude decreased more slowly than that of the PHE, then the balance between this effect and the PHE would change as the temperature increases, with the PHE becoming less predominant at higher temperature, leading to the extra signal observed. One possibility for such a signal would be a contribution to the magnetoresistance from a small out-of-plane magnetic field B_{\perp} , due to a misalignment between the sample's plane and the rotation plane of the rotator. Such a misalignment would result in a 2π -periodic variation of B_{\perp} around $B_{\perp} = 0$, as the sample is rotated. This would result in a 2π -periodic contribution to R_{yx} , as the Hall resistance is odd in out-of-plane field, but would give a π -periodic contribution in R_{xx} , as the longitudinal resistance is even in out-of-plane field. A tilt of the sample with respect to the rotation plane would therefore result in an additional π -periodic contribution in R_{xx} , with no such additional contribution in

R_{xx} . Depending on the axis of this tilt with respect to the orientation of the current in the sample, this additional contribution would either add up to or cancel out some of the oscillation due to the PHE. We note that a misalignment of the rotation plane with respect to the magnetic field axis would result in a constant out-of-plane field, independent on the angular position of the sample, and would therefore not have an influence on the π -periodic signal. As the PHE and the longitudinal magnetoresistance (LMR) are not expected to fully share a common physical origin in our material, they have no reason to share a similar temperature dependence. It is therefore possible that the LMR has a slower decrease in temperature than the PHE, and could account for the additional oscillation seen in our measurements.

DISCUSSION

The band structure of t-PtBi₂ is quite complex from a topological perspective. As we reported previously, DFT calculations show that t-PtBi₂ is a Weyl semi-metal with 12 symmetry-related Weyl nodes (see Figure 1) close to the the Fermi energy [8] (~ 45 meV above E_F). This prediction was later experimentally confirmed by ARPES [10] and STM [11] experiments, in which the Fermi arcs (topological surface states associated with the Weyl nodes) were observed, although no transport signature of the topology of t-PtBi₂ nanostructures (aside from the anomalous planar Hall effect [12] has been reported as of now. Since then, more detailed calculations [12] have found the existence of 3 additional groups of 12 (each) symmetry-related Weyl nodes at higher energies, at ~ 141 meV, ~ 300 meV and ~ 320 meV above E_F respectively, as well as topological nodal lines - 1D continuous band touchings - in the band structure between the HOMO and LUMO bands (see [12], and SM). While assigning a quantitative weight to the contributions of each such topological features to the observed PHE is far beyond the scope of this study, the contribution from the group of 12 Weyl nodes closest to the Fermi energy is likely to dominate (see more detailed discussion in SM).

The most well known transport signature of topological semi-metals is the negative longitudinal magnetoresistance, which is associated with the chiral anomaly [21]. However, it has been recently understood that in Weyl semi-metals effects of orbital magnetic moments could result both in a positive longitudinal magnetoresistance [22] and in a positive transversal magnetoresistance [20] when considering tilted Weyl cones. The anisotropy in these responses is expected to lead to a PHE that therefore represents one of the main transport signature in topological semi-metals. It is important to point out that the observation of a PHE in non-magnetic mate-

rials does not necessarily imply the presence of topological degeneracies. The Lorentz-force induced orbital magnetoresistance [23] is also expected to be anisotropic due to cancellation of Lorentz force with collinear electric and magnetic fields and can therefore yield a PHE. In this regard, it is important to note that a very large magnetoresistance (with out-of-plane magnetic field) has been reported in PtBi₂ [8]. We can thus expect the orbital magnetoresistance to be significant, and therefore its anisotropies could contribute to a PHE.

Nonetheless, our measurements are consistent with the predictions of Weyl physics in PtBi₂, and furthermore all our results can be understood in that context, without needing to invoke additional effects. The observation of a PHE in PtBi₂ therefore reinforces with charge-transport previous observations from spectroscopy techniques [10, 11] as to its Weyl nature.

CONCLUSION

In this paper, we presented the first measurement of the planar Hall effect in nanostructure of the vander-Waals layered non-magnetic type-I Weyl semi-metal trigonal-PtBi₂, and study their dependence in magnetic field and temperature. The discovery of a PHE in PtBi₂ is significant, as it is an expected signature of Weyl semi-metals. We have found that the PHE is present already at magnetic fields as low as 1 T, and is robust up to room temperature. We also unveiled some deviations from the theoretical expectations for the PHE in Weyl semi-metals, with a sub-quadratic field dependence of the amplitude, which may originate from a combination of the Weyl-cones' tilt (e.g. from some type-II Weyl nodes originating from the nodal lines) and a deviation from the simple sine-wave model when the amplitude of the oscillations is large.

Overall, this study reinforces our understanding of the quantum geometry of trigonal-PtBi₂, which is of particular interest in the context of the recent discovery of superconductivity in this material, with two-dimensional superconductivity reported in bulk nanostructures, and surface Fermi-arc supported superconductivity seen in ARPES.

METHODS AND SM

Methods

Sample Preparation

The high-quality single crystals of PtBi₂ were synthesized using the self-flux technique, as described in [24]. The single crystals we measured could reach Residual Resistance Ratios (RRR) up to $RRR \sim 130$, as shown in

[8] (in SM). Thin flakes, with widths exceeding 10 μm and thicknesses ranging from a few dozen to several hundred nanometers, were obtained via mechanical exfoliation. Electrical contacts were fabricated using Cr/Au deposition through standard e-beam lithography methods. To remove surface oxidation before metal deposition, a light Ar etching process was performed by IBE.

The primary sample examined in this study, labeled *D1*, has a thickness of 70 nm. Additional data includes complementary results from a second sample, *D2* (126 nm thick). A third sample, *D4* (41 nm), was measured at low temperatures in a vector magnet (see Figure 3) but was unfortunately damaged before further measurements could be conducted.

No indications of aging effects were observed between the two experimental sessions, as confirmed in *D1* by the stability of the residual resistance ratio ($RRR = R(300\text{K})/R(4\text{K})$), which remained unchanged (see [12], SM). The RRR of the different samples, as reported in [8], was 8.7 for *D1* (70nm), 13.6 for *D2* (126nm) and 4.7 for *D4* (41nm).

Measurement Setup

The sample is arranged in a conventional Hall-bar geometry. A current is applied between the source and drain, as illustrated in Figure 3.a,b,c.

Longitudinal and transverse resistances, shown in blue and red respectively, are measured along and perpendicular to the sample with respect to the current direction.

Vector magnet measurements

The PHE in t-PtBi₂ was measured first in 2-dimensional in-plane magnetic field mappings of the longitudinal and transverse resistance at 1 K with a 3D vector magnet (Figure 3). The resistance was measured using external lock-in amplifiers, with an AC current of 20 μA at a frequency of 113 Hz, with an integration time of 300 ms.

To extract the angular dependence of the resistance from the mappings (at a fixed field B_0 between 500 mT and 1.5 T), we considered all points within the annulus centered around $B_0 : |B - B_0| < 20$ mT. These points were then ordered by their angle φ , and the resulting list was interpolated to a uniform 1° step. The width of the annulus was selected to be large enough to include enough points (over the full angular range) for the analysis to be meaningful, while being small enough to avoid the data at "fixed field" being over-influenced by the field dependence of the PHE.

Variable temperature insert measurements

Additional measurements were performed using a Dynacool 14T PPMS, in a mechanical 2D rotator-equipped insert.

By changing the sample's orientation with the rotator, the angle φ between the applied current and the fixed-axis magnetic field could be varied continuously over a full 360° range, where φ represents the angle between the magnetic and electric fields.

Resistances were measured with external lock-in amplifiers, by injecting an AC current of $100 \mu\text{A}$ at a frequency of 927.7 Hz , and an integration time of 300 ms . At these low currents, thermal effects are negligible. For sample *D1*, measurements were taken at $T = 5 \text{ K}$ for magnetic fields of $B = 1, 2, 3, 4, 5, 6, 7, 10 \text{ T}$, and at $B = 14 \text{ T}$ for temperatures $T = 5, 10, 20, 50, 300 \text{ K}$. At each angular position, the resistance was measured 10 times and then averaged. An angular step of 1° was used for these measurements. Identical measurement conditions were applied to sample *D2*.

For sample *D1*, higher-precision measurements were carried out at $T = 5 \text{ K}$ and $B = 14 \text{ T}$, as well as at $B = 14 \text{ T}$ for $T = 100, 200 \text{ K}$. These measurements involved averaging over 40 points at each angular position, with a 0.5° angular step. The data were then interpolated to a 1° step to ensure uniform analysis across all (B,T) measurements.

A high-frequency noise component appears superimposed on the π -periodic oscillation for both *D1* and *D2*, with a stronger presence in the latter. This noise likely originates from the mechanical rotator: when the stepper motor at the top of the measurement stick rotates by a small angle (e.g., 1°), the corresponding movement of the rotator inside the cryostat is not perfectly uniform, fluctuating around the intended step size.

Since the rotator's angle is measured at the top of the stick (rather than the sample's exact position at the bottom), these discrepancies introduce minor deviations in the planar Hall effect (PHE) signal from an ideal π -periodic oscillation. These artifacts are reproducible and diminish with increasing temperature, which is consistent with expected mechanical inaccuracies in the rotator.

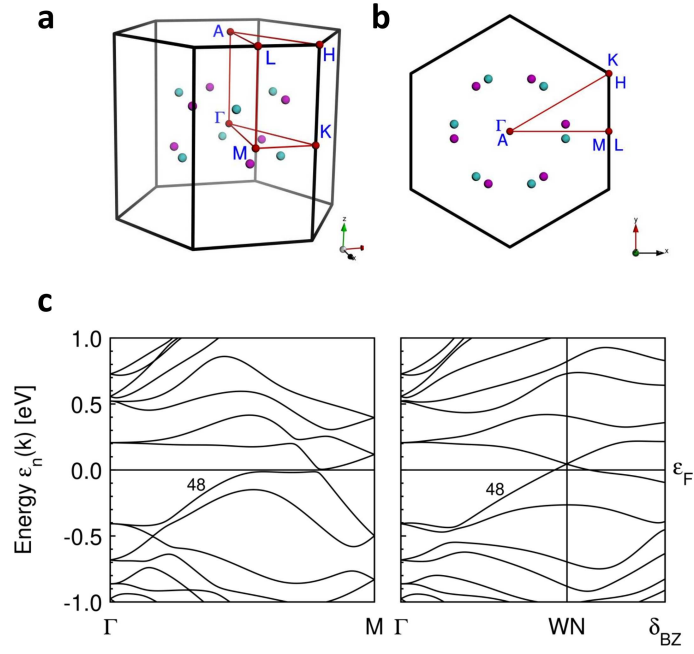


FIG. 1. **a,b**: Brillouin zone showing the 12 symmetry-related Weyl nodes in band 48 (see [12] closest to the Fermi level, with colour-encoded chirality). **c**: Band structure along the ΓM line (left panel) and from Γ to the Brillouin zone boundary through the blue Weyl node closest to the ΓM line.

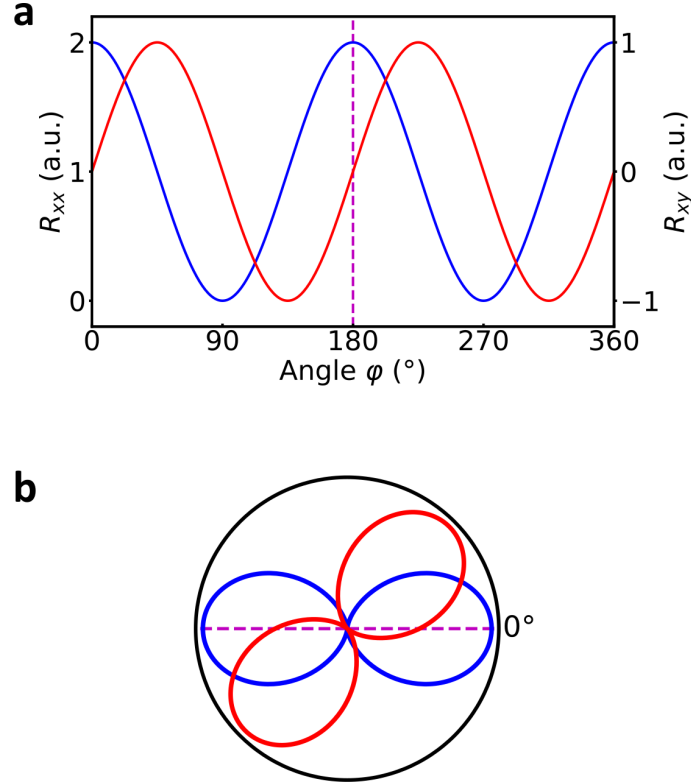


FIG. 2. **a,b**: Typical angular dependence of the conventional planar Hall effect, in Cartesian (**a**) and polar (**b**) coordinates. Both the longitudinal (anisotropic magnetoresistance, R_{xx} , blue) and transverse (planar Hall effect, R_{yx} , red) resistances exhibit a π -periodic angular dependence, with a $\pi/4$ -offset between them. The origin of the oscillation is set by the direction of the electric field (current).

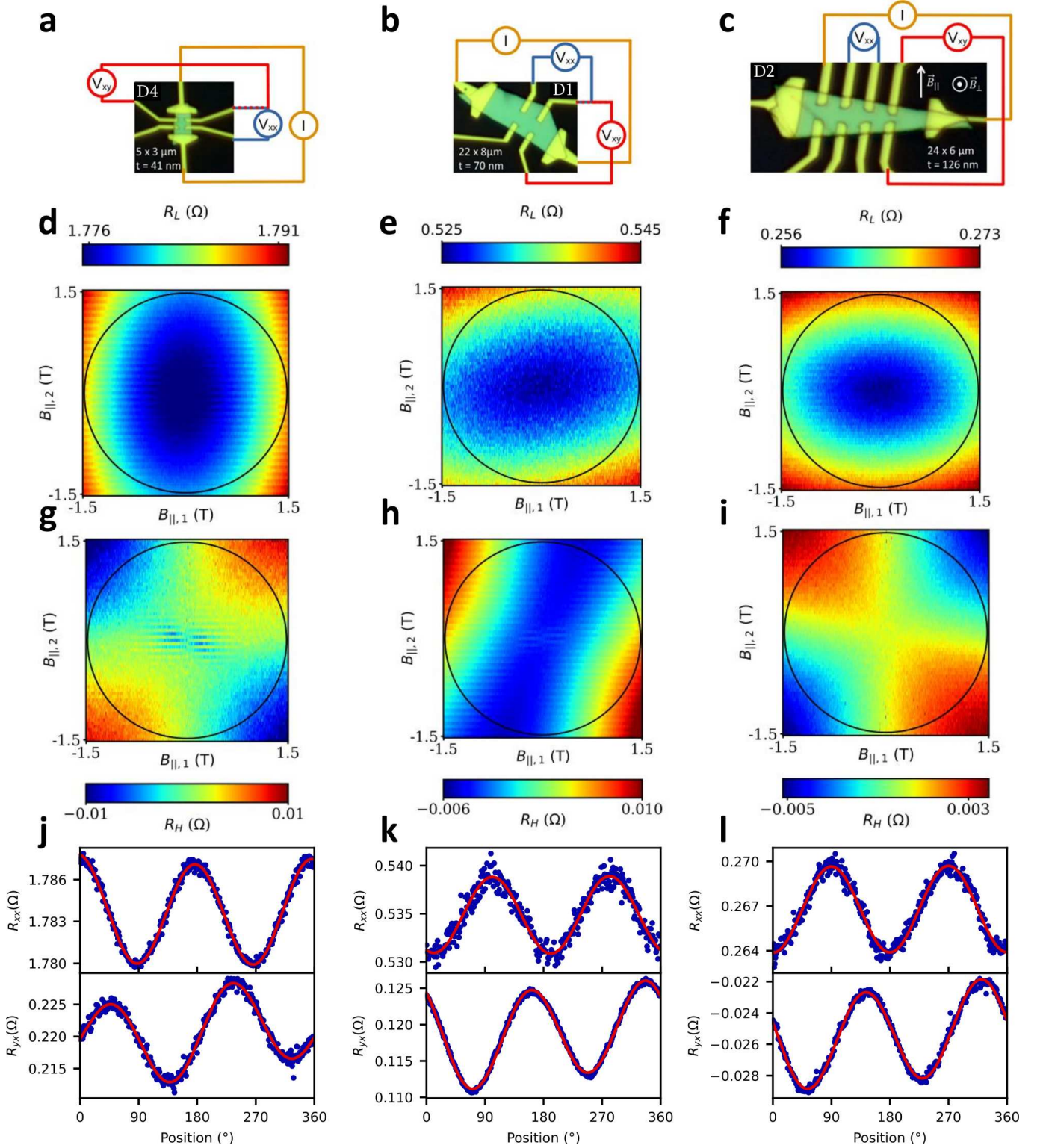


FIG. 3. **a,b,c**: Optical pictures and sample configurations for D4 (41 nm), D1 (70 nm) and D2 (126 nm). The measurements related to each sample is shown below it. **d-i**: In-plane magnetic field ($B_y - B_z$) mappings of the longitudinal (R_{xx} , d,e,f) and transverse (R_{yx} , g,h,i) resistances. All mappings were measured simultaneously by sweeping $B_{||,1}$ at fixed $B_{||,2}$, and increasing $B_{||,2}$ in steps of 50 mT. All mappings show the expected four-fold symmetry expected for the PHE, with sample-orientation-dependent phase and $\pi/4$ shift between longitudinal and transverse configurations. **j-l**: Angular dependence of R_{xx} (top panels) and R_{yx} (bottom panels) extracted from the mappings **d-i**, for a field $B = 1.5$ T corresponding to the black circles. The data is well fitted by the PHE model (in red, see Equation 4). The phase of the oscillations in each sample can be correlated to the presumed current orientation in the sample.

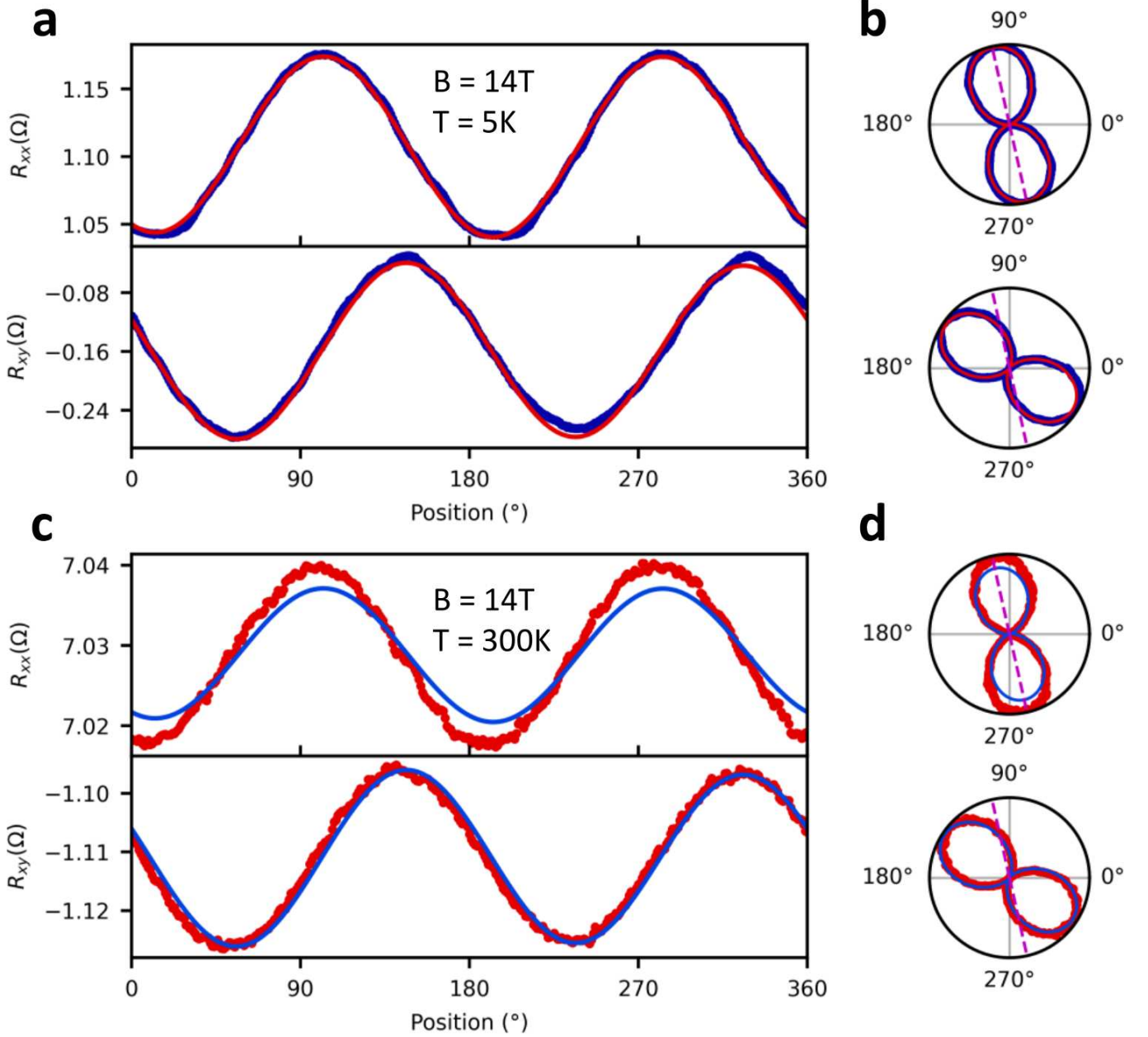


FIG. 4. **a,c:** Angular dependence at 14 T and 5 K (a) or 300 K (c) of the longitudinal (R_{xx} , top panels) and transverse (R_{yx} , bottom panels) resistances for sample D1, in Cartesian coordinates. Fits to the PHE model (Equation 4) are shown in red (a) and blue (c). **b,d:** Same data as in **a,c**, in polar coordinates. The dashed-line represents the orientation of the current estimated from the data. ^a

^a We note that, although the raw data shown is the same as in [12], the fits in the present figure are different from that other study, as the latter were unconstrained π - and 2π -periodic signals, while the presents ones are heavily constrained, as discussed in the main text.

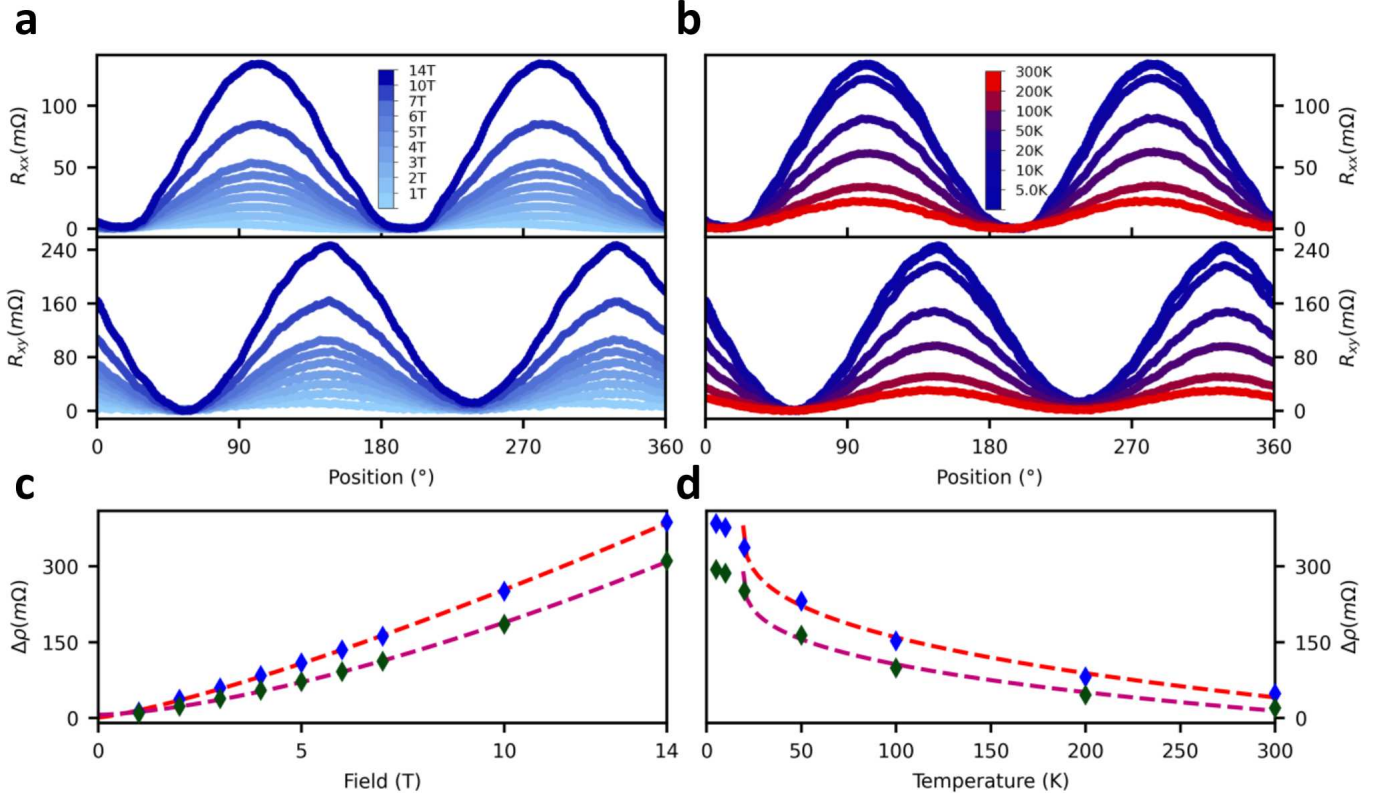


FIG. 5. **a,b:** Angular dependence of the longitudinal (R_{xx} , top panels) and transverse (R_{yx} , bottom panels) resistances of samples D1 at 5K and multiple fields from 1T to 14T (a) and at 14T and multiple temperatures from 5K to 300K (b). The plots are shifted vertically for visibility, to share a minimum at 0 Ω . **c,d:** Field (c) and temperature (d) dependence of the PHE amplitude $\Delta\rho$ extracted from fits of the data in (a,b) with Equation 4 for samples D1 (blue diamonds and dashed-red line, respectively), and for sample D2 (green diamonds and dashed-magenta line, respectively, see SM). The field dependence of $\Delta\rho$ is well fitted with a sub-quadratic power law for both samples. The temperature dependence of $\Delta\rho$ cannot be fitted with an exponential decay law, and is fitted with a power law.

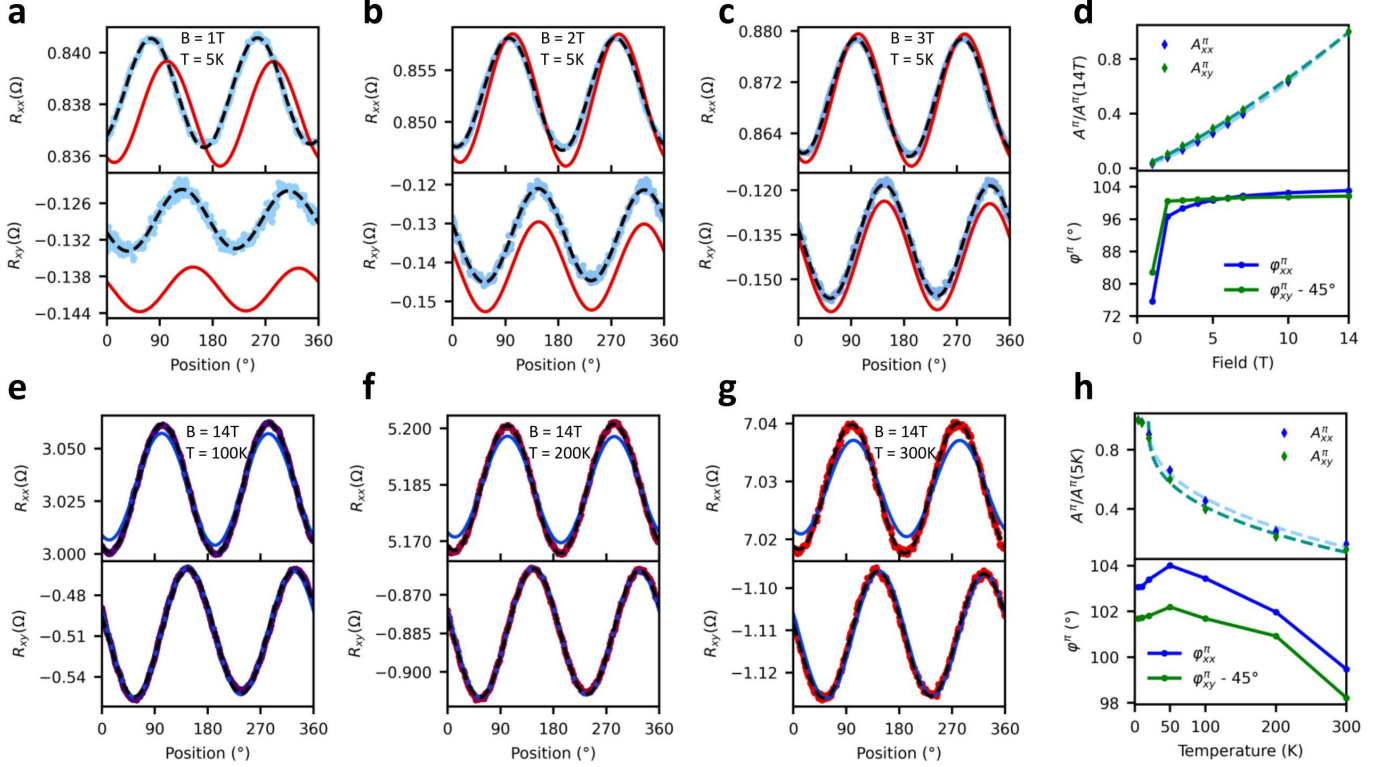


FIG. 6. **a,b,c**: Angular dependence of the longitudinal (R_{xx} , top panels) and transverse (R_{yx} , bottom panels) resistances at 5 K and 1T (a), 2T (b) and 3T (c). As the result of dephasing and unaccounted-for offset, the constrained fits of the PHE model (Equation 4, in red) start deviating from the measurements at low fields. The data can still be fitted very well with an unconstrained π -periodic fit (in dashed black). **d**: Field dependence of the amplitude (top panel, renormalized to its value at 14T) and phase (bottom panel) of the unconstrained fits of the longitudinal (R_{xx} , blue) and transverse (R_{yx} , green) resistances. The renormalized amplitudes of the oscillations in R_{xx} and R_{yx} have the same field dependence, as expected for the PHE, however the phase of the oscillations can change significantly with the magnetic field. **e,f,g**: Angular dependence of the longitudinal (R_{xx} , top panels) and transverse (R_{yx} , bottom panels) resistances at 14 T and 100 K (e), 200 K (f) and 300 K (g). The constrained fits of the PHE model (Equation 4, in blue) start deviating from the measurements in R_{xx} at high temperature, as the amplitude of the oscillations are smaller than anticipated from those in R_{yx} . The data can still be fitted very well with an unconstrained π -periodic fit (in dashed black). **h**: Temperature dependence of the amplitude (top panel, renormalized to its value at 5 K) and phase (bottom panel) of the unconstrained fits of the longitudinal (R_{xx} , blue) and transverse (R_{yx} , green) resistances. The renormalized amplitudes of the oscillations in R_{xx} and R_{yx} have a different dependence in temperature, as the amplitude in R_{xx} decreases more slowly than that in R_{yx} . The phase of the oscillations changes slightly with the temperature.

-
- * arthur.veyrat@universite-paris-saclay.fr
† cortex@unisa.it
‡ j.dufouleur@ifw-dresden.de
- [1] X. Wan, A. M. Turner, A. Vishwanath, and S. Y. Savrasov, *Physical Review B - Condensed Matter and Materials Physics* **83**, 1 (2011).
- [2] A. A. Burkov, *Physical Review B* **96**, 041110 (2017).
- [3] S. Nandy, G. Sharma, A. Taraphder, and S. Tewari, *Physical Review Letters* **119**, 1 (2017).
- [4] N. Kumar, S. N. Guin, C. Felser, and C. Shekhar, *Physical Review B* **98**, 1 (2018), arXiv:1711.04133.
- [5] R. Singha, S. Roy, A. Pariari, B. Satpati, and P. Mandal, *Physical Review B* **98**, 081103 (2018), arXiv:1806.08287.
- [6] Q. Liu, F. Fei, B. Chen, X. Bo, B. Wei, S. Zhang, M. Zhang, F. Xie, M. Naveed, X. Wan, F. Song, and B. Wang, *Phys. Rev. B* **99**, 155119 (2019).
- [7] A. A. Taskin, A. A. Taskin, A. A. Taskin, H. F. Legg, F. Yang, S. Sasaki, S. Sasaki, Y. Kanai, K. Matsumoto, A. Rosch, and Y. Ando, *Nature Communications* **8**, 1340 (2017).
- [8] A. Veyrat, V. Labracherie, D. L. Bashlakov, F. Caglieris, J. I. Facio, G. Shipunov, T. Charvin, R. Acharya, Y. Naidyuk, R. Giraud, J. van den Brink, B. Büchner, C. Hess, S. Aswartham, and J. Dufouleur, *Nano Lett.* 10.1021/acs.nanolett.2c04297 (2023).
- [9] S. Schimmel, Y. Fasano, S. Hoffmann, J. Puig, G. Shipunov, D. Baumann, S. Aswartham, B. Büchner, and C. Hess, High-TC surface superconductivity in topological Weyl semimetal t-PtBi2 (2023), arXiv:2302.08968 [cond-mat].
- [10] A. Kuibarov, O. Suvorov, R. Vocaturo, A. Fedorov, R. Lou, L. Merkwitz, V. Voroshnin, J. I. Facio, K. Koepernik, A. Yaresko, G. Shipunov, S. Aswartham, J. V. D. Brink, B. Büchner, and S. Borisenko, *Nature* **626**, 294 (2024).
- [11] S. Hoffmann, S. Schimmel, R. Vocaturo, J. Puig, G. Shipunov, O. Janson, S. Aswartham, D. Baumann, B. Büchner, J. van den Brink, Y. Fasano, J. I. Facio, and C. Hess, Fermi arcs dominating the electronic surface properties of trigonal PtBi₂ (2024), arXiv:2407.15790 [cond-mat].
- [12] A. Veyrat, K. Koepernik, L. Veyrat, G. Shipunov, I. Kovalchuk, S. Aswartham, J. Qu, A. Kumar, M. Ceccardi, F. Caglieris, N. Pérez, R. Giraud, B. Büchner, J. van den Brink, C. Ortix, and J. Dufouleur, *Nature Communications* **16**, 6711 (2025).
- [13] W. Thomson, *Proc. R. Soc. Lond.* **8**, 546 (1857).
- [14] K. Hong and N. Giordano, *Phys. Rev. B* **51**, 9855 (1995).
- [15] A. A. Burkov, *Journal of Physics Condensed Matter* **27**, 10.1088/0953-8984/27/11/113201 (2015), arXiv:1502.07609.
- [16] P. Li, C. Zhang, Y. Wen, L. Cheng, G. Nichols, D. G. Cory, G.-X. Miao, and X.-X. Zhang, *Physical Review B* **100**, 205128 (2019).
- [17] D. D. Liang, Y. J. Wang, W. L. Zhen, J. Yang, S. R. Weng, X. Yan, Y. Y. Han, W. Tong, W. K. Zhu, L. Pi, and C. J. Zhang, *AIP Advances* **9**, 055015 (2019).
- [18] J. Meng, H. Xue, M. Liu, W. Jiang, Z. Zhang, J. Ling, L. He, R. Dou, C. Xiong, and J. Nie, *J. Phys.: Condens. Matter* **32**, 015702 (2019).
- [19] J. G. Glusckke, J. Seidl, H. H. Tan, C. Jagadish, P. Caroff, and A. P. Micolich, *Nanoscale* **12**, 20317 (2020).
- [20] K. Das and A. Agarwal, *Phys. Rev. B* **100**, 085406 (2019), arXiv:1903.01205 [cond-mat.mes-hall].
- [21] D. T. Son and B. Z. Spivak, *Physical Review B - Condensed Matter and Materials Physics* **88**, 1 (2013), arXiv:1206.1627.
- [22] A. Knoll, C. Timm, and T. Meng, *Phys. Rev. B* **101**, 201402 (2020), arXiv:1912.07852 [cond-mat.mes-hall].
- [23] Y. Cui, Z. Li, H. Chen, Y. Wu, Y. Chen, K. Pei, T. Wu, N. Xie, R. Che, X. Qiu, Y. Liu, Z. Yuan, and Y. Wu, *Science Bulletin* **69**, 2362 (2024).
- [24] G. Shipunov, I. Kovalchuk, B. R. Piening, V. Labracherie, A. Veyrat, D. Wolf, A. Lubk, S. Subakti, R. Giraud, J. Dufouleur, S. Shokri, F. Caglieris, C. Hess, D. V. Efremov, B. Büchner, and S. Aswartham, *Physical Review Materials* **4**, 124202 (2020), arXiv:2002.03976.

Planar Hall effect in nanostructures of trigonal-PtBi₂: Supplementary Materials

Arthur Veyrat,^{1,2,3,*} Klaus Koepf, ^{1,2} Louis Veyrat,^{1,2,4} Grigory Shipunov,^{1,2}
 Iryna Kovalchuk,^{5,1} Saicharan Aswartham,^{1,2} Jiang Qu,^{1,2} Ankit Kumar,^{1,2} Michele
 Ceccardi,^{6,7} Federico Caglieris,⁷ Nicolás Pérez Rodríguez,^{1,2} Romain Giraud,^{1,2,8} Bernd
 Büchner,^{1,2,9} Jeroen van den Brink,^{1,2,9} Carmine Ortix,^{10,†} and Joseph Dufouleur^{1,2,11,‡}

¹Leibniz Institute for Solid State and Materials Research (IFW Dresden), Helmholtzstraße 20, D-01069 Dresden, Germany

²Würzburg-Dresden Cluster of Excellence ct.qmat, Dresden, Germany

³Laboratoire de Physique des Solides (LPS Orsay), 510 Rue André Rivière, 91400 Orsay, France

⁴CNRS, Laboratoire National des Champs Magnétiques Intenses, Université Grenoble-Alpes,
 Université Toulouse 3, INSA-Toulouse, EMFL, 31400 Toulouse, France

⁵Kyiv Academic University, 03142 Kyiv, Ukraine

⁶Department of Physics, University of Genoa, 16146 Genoa, Italy

⁷CNR-SPIN Institute, 16152 Genoa, Italy

⁸Université Grenoble Alpes, CNRS, CEA, Grenoble-INP, Spintec, F-38000 Grenoble, France

⁹Department of Physics, TU Dresden, D-01062 Dresden, Germany

¹⁰Dipartimento di Fisica “E. R. Caianiello”, Università di Salerno, IT-84084 Fisciano (SA), Italy

¹¹Center for Transport and Devices, TU Dresden, D-01069 Dresden, Germany

SUPPLEMENTARY MATERIALS

Resistivity in the planar Hall effect

It is expected from the theory [1] that the planar Hall effect (PHE) component of the conductivity follows the angular dependence

$$\begin{aligned}\sigma_{xx}^{\text{PHE}}(\varphi) &= \sigma_{\perp} + \Delta\sigma \cos^2 \varphi, \\ \sigma_{yx}^{\text{PHE}}(\varphi) &= \Delta\sigma \cos \varphi \sin \varphi,\end{aligned}\tag{1}$$

with $\Delta\sigma = \sigma_{\parallel} - \sigma_{\perp}$ the amplitude of the oscillation, σ_{\perp} and σ_{\parallel} the conductivity when the in-plane magnetic field is orthogonal or parallel to the electric field (i.e. the current), and φ the angle between the magnetic field and the current. When the PHE originates from the chiral anomaly in Weyl semimetals, it is expected that σ_{\perp} is constant in magnetic field, with $\sigma_{\perp} = \sigma_D$ the drude conductivity, and $\sigma_{\parallel} = \sigma_D + a \cdot B^2$ increases with magnetic field. In order to obtain the resistivity matrix, we must inverse the conductivity matrix $\sigma = \begin{pmatrix} \sigma_{xx} & \sigma_{xy} \\ \sigma_{yx} & \sigma_{yy} \end{pmatrix}$. From Onsager relations, we have $\sigma_{yx}(B) = \sigma_{xy}(-B)$. Since the magnetic field is in the plane, $\sigma_{xy}(-B, \varphi) = \sigma_{xy}(B, \varphi + \pi) = \sigma_{xy}(B, \varphi)$ as σ_{xy} is π -periodic. Hence, we have $\sigma_{yx}(B) = \sigma_{xy}(B)$. We can also note that σ_{yy} can be expressed similarly to σ_{xx} by simply exchanging σ_{\parallel} and σ_{\perp} : $\sigma_{yy}(\varphi) = \sigma_{\parallel} - \Delta\sigma \cos^2 \varphi$.

We can then invert the conductivity matrix to obtain the resistivity matrix $\rho = \sigma^{-1} = \begin{pmatrix} \rho_{xx} & \rho_{xy} \\ \rho_{yx} & \rho_{yy} \end{pmatrix}$, with

$$\begin{aligned}\rho_{xx} &= \frac{\sigma_{yy}}{\sigma_{xx} \cdot \sigma_{yy} - \sigma_{xy}^2} = \frac{\sigma_{yy}}{\sigma_{\perp} \cdot \sigma_{\parallel}}, \\ \rho_{xy} &= \frac{-\sigma_{xy}}{\sigma_{xx} \cdot \sigma_{yy} - \sigma_{xy}^2} = \frac{-\sigma_{xy}}{\sigma_{\perp} \cdot \sigma_{\parallel}} = \rho_{yx}\end{aligned}\tag{2}$$

From Equation 2, we recover the shape of the resistivity from [2]:

$$\begin{aligned}\rho_{xx}(\varphi) &= \rho_{\perp} - \Delta\rho \cos^2 \varphi, \\ \rho_{yx}(\varphi) &= \Delta\rho \cos \varphi \sin \varphi,\end{aligned}\tag{3}$$

with $\Delta\rho = \rho_{\perp} - \rho_{\parallel}$, $\rho_{\perp} = 1/\sigma_{\parallel}$ and $\rho_{\parallel} = 1/\sigma_{\perp}$.

However, while the amplitude of the oscillations in conductivity $\Delta\sigma \propto B^2$ is quadratic in field, this is only true at low field for the resistivity:

$$\Delta\rho = \frac{\sigma_{\perp} - \sigma_{\parallel}}{\sigma_{\perp} \cdot \sigma_{\parallel}} = -\frac{1}{\sigma_D} \cdot \frac{a/\sigma_D \cdot B^2}{1 + a/\sigma_D \cdot B^2}.\tag{4}$$

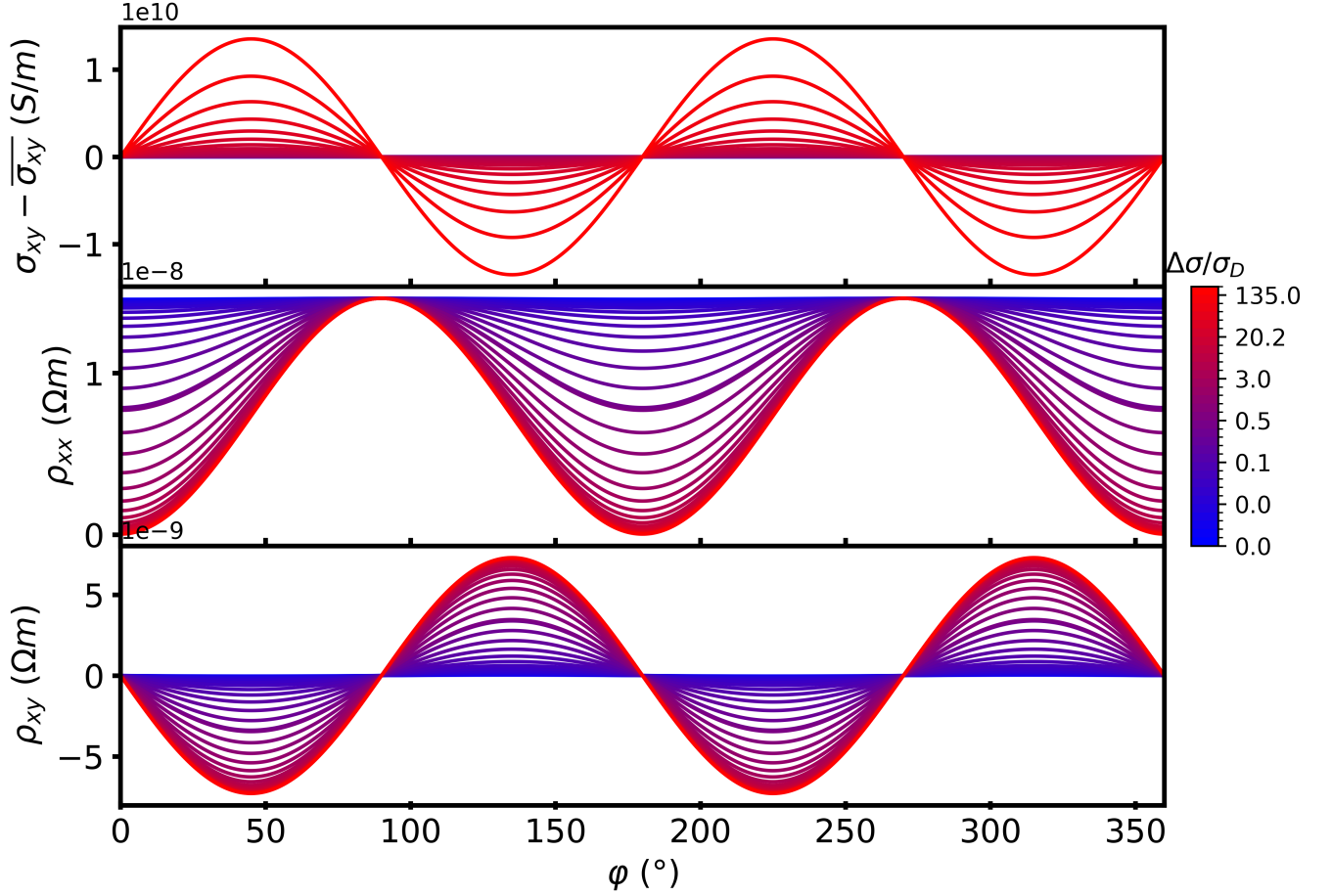


FIG. 1. Simulations showing the angular dependence of the PHE signal in the transverse conductivity (top, vertically offset for visibility), the longitudinal resistivity (middle) and transverse resistivity (bottom), at different magnetic fields from 0.1T (blue) to 300T (red). The corresponding ratio $\Delta\sigma/\sigma_D$ are shown on the right. The parameters used in these simulations are given in section

When $a \cdot B^2/\sigma_D \ll 1$, we recover the field dependence from [2], $\Delta\rho \propto B^2$, but when $a \cdot B^2/\sigma_D \sim 1$, or alternatively, when $\Delta\sigma \sim \sigma_D$, this approximation breaks down and the oscillations in resistivity begin saturating.

We can estimate at which magnetic field we would expect to see this saturation behaviour in our samples, for instance in *D2*. We can consider that $\sigma_D = 1/\rho_{\perp}(0T) = 1/R_{xx}(0T) * \frac{l}{A}$, with l the distance between the longitudinal contacts, and $A = w * t$, with w, t the width and thickness of the sample, respectively. As a rough estimate, we can take $R_{xx}(0T) \sim 0.836 \Omega$, $l \sim 20 \mu m$, $w \sim 5 \mu m$ and $t \sim 70 nm$, which gives $\sigma_D \sim 6.835 S/m$. In order to get $\Delta\rho(14T) = 387 m\Omega * \frac{l}{A} \sim 6.7e^{-9} \Omega m$, we choose $a = 3e^5 S/m$ in the quadratic field-dependence of σ_{\parallel} . The field dependence of the PHE predicted with these parameters is shown in Figure 1 and Figure 2 until 300T.

As expected, the oscillations in resistivity remain sinusoidal over the entire field range, and their amplitude saturates at high field. At low field (i.e. $B < 14 T$), we can fit $\Delta\rho$ well with a subquadratic power law: $\Delta\rho(B) \sim b * B^c$, with $b \sim 1.35e^{-10} \Omega m$ and $c \sim 1.50$, which is close to the value obtained in our measurements. Although this model is quite simple, as it assumes a simple quadratic field dependence of $\Delta\sigma$ (as in the pure chiral anomaly case in type-I Weyl semimetals), we can see that 14T is close to the inflection point of the field dependence. Even if the field dependence of $\Delta\sigma$ is slightly slower (i.e. subquadratic), measurements in high-field facilities (e.g. up to 60-100T) should show the saturation. One interesting thing to note is that samples with lower resistivities (i.e. higher conductivities) should show a saturation at higher fields than samples with higher resistivities.

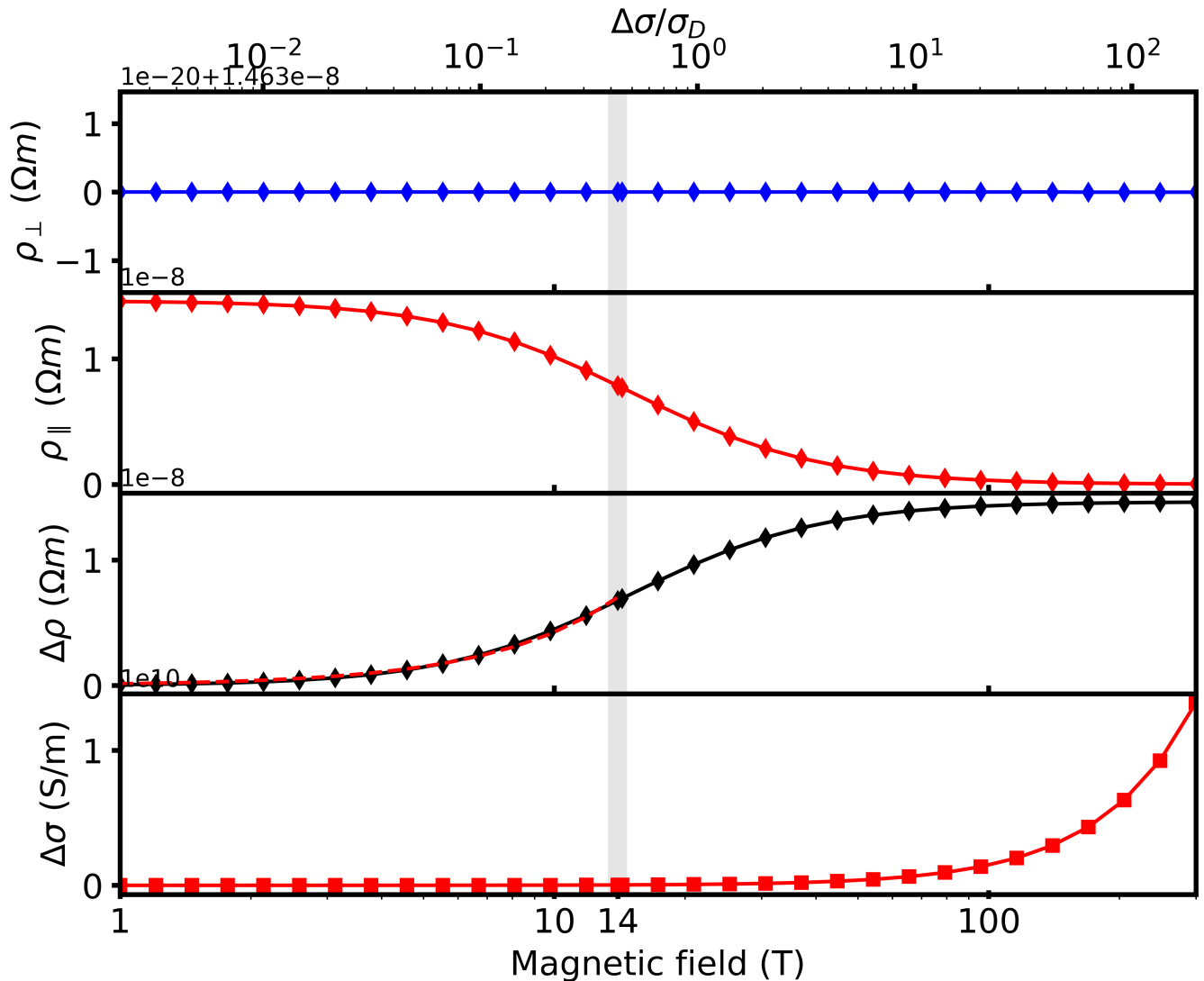


FIG. 2. Field dependence of different parameters of the PHE obtained from fitting the simulations of Figure 1 with Equation 3. The power fit of $\Delta\rho$ is shown in dashed red. The ratio $\Delta\sigma/\sigma_D$ corresponding to the magnetic field is shown at the top. The vertical grey line indicates a magnetic field of 14T.

Discussion on the relative contributions to the PHE

As mentioned in the main text, detailed DFT calculations [3] have found the existence of 3 additional groups of 12 (each) symmetry-related Weyl nodes at high energies, at ~ 141 meV, ~ 300 meV and ~ 320 meV above E_F respectively. In the following, these 4 groups are referred to as the "zero-field" Weyl nodes, as they exist even in the absence of an external magnetic field. Furthermore, these recent calculations also reveal the existence of topological nodal lines - 1D continuous band touchings - in the band structure between the HOMO and LUMO bands (see [3], SM). When a mirror symmetry-breaking magnetic field is applied, these nodal lines convert into a total of 6 additional groups of 6 Weyl nodes (each) along the nodal lines and at various energies (at ~ -655 meV, ~ -497 meV, ~ -80 meV, ~ 202 meV, ~ 285 meV, and ~ 320 meV with respect to E_F), giving rise to an anomalous planar Hall effect (APHE), which we studied in details in [3]. In the following, these 6 groups are referred to as the "field-generated" Weyl nodes, as they only appear when an external magnetic field is applied.

It is extremely difficult to quantitatively differentiate the contributions to the PHE of each groups of Weyl nodes. It can reasonably be assumed that, out of the four groups of zero-field Weyl nodes, the one closest to the Fermi energy (G3 in [4], first predicted in [4]) will contribute the most. Indeed, the contribution of the chiral anomaly to the PHE

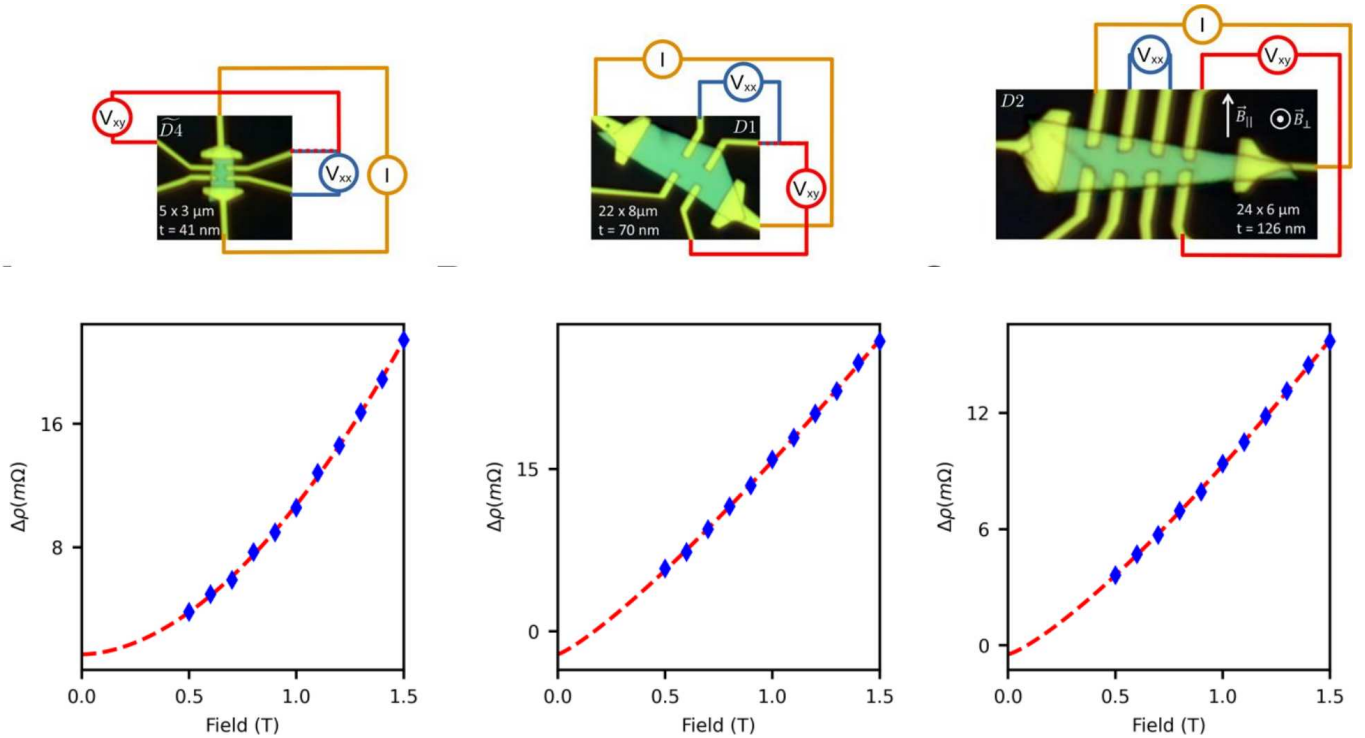


FIG. 3. **a,b,c**: Optical pictures and sample configurations for D3 (41 nm), D1 (70 nm) and D2 (126 nm). The measurements related to each sample is shown below it. **d,e,f**: Amplitudes of the π -periodic oscillations extracted from (d,e,f), for both longitudinal and transverse resistances, at various magnetic fields between 0.5 T and 1.5 T, and their field dependences are fitted to power laws (dashed lines).

comes from the accumulation of carriers around one Weyl cone with a given chirality, and a corresponding depletion of carriers around a Weyl cone with the opposite chirality [5]. When the Fermi energy exceeds the Lifshitz-transition energy, inter-cone scattering will tend to reduce this imbalance in chiral carriers. With WN close in k -space, such inter-cone scattering will occur via long-range disorder, and may therefore be very efficient. This suggests a stronger contribution to the PHE from the Weyl nodes closest to E_F . However, when the WN are far in k -space, the main mechanism behind inter-cone scattering will be due to short-range disorder, which might be far less efficient. As the k -space distance between the field-generated Weyl nodes (from the nodal lines, see [3]) is unusually large (by the very nature of their creation mechanism), we cannot dismiss the contribution of these field-generated Weyl nodes simply due to their distance to the Fermi energy. On the other hand, as the strength of the PHE grows with the square of the Fermi velocity of the Weyl cones [2], one could speculate that, at least in the weak field limit, the zero-field Weyl nodes should give a stronger contribution to the PHE than the Weyl nodes due to conversion of nodal lines, as one could naively expect the Fermi velocity of these field-generated nodes to be roughly proportional to the magnetic field to recover line degeneracies in the $B \rightarrow 0$ limit. Therefore, the field-generated Weyl nodes might not contribute much to the PHE. Further research is therefore needed to determine the relative contribution of the different Weyl nodes in this system.

Reproduced from previous publications on the same devices

* arthur.veyrat@universite-paris-saclay.fr

† cortix@unisa.it

‡ j.dufouleur@ifw-dresden.de

[1] S. Nandy, G. Sharma, A. Taraphder, and S. Tewari, Physical Review Letters **119**, 1 (2017).

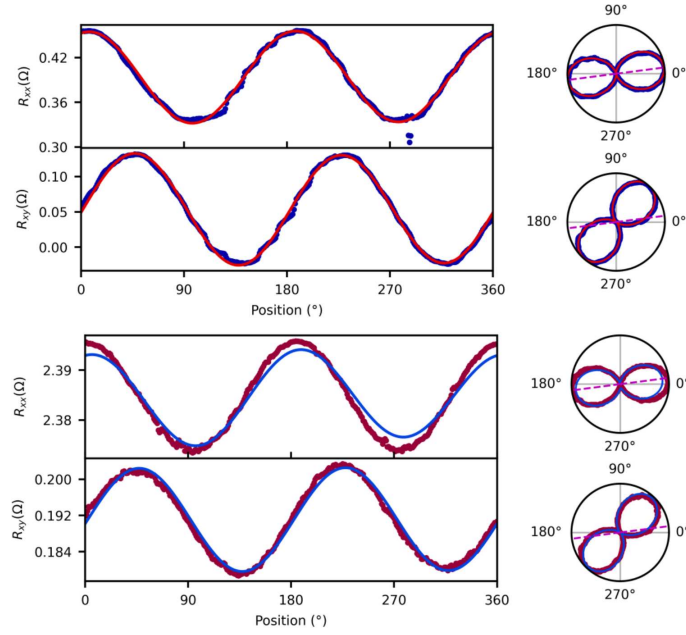


FIG. 4. **a,c**: Angular dependence at 14 T and 1.9 K (a) and 200 K (c) of the longitudinal (R_{xx} , top panels) and transverse (R_{yx} , bottom panels) resistances for sample D2, in Cartesian coordinates. Fits to the PHE model are shown in red (a) and blue (c). **b,d**: Same data as in **a,c**, in polar coordinates. The dashed-line represents the orientation of the current estimated from the data.

- [2] A. A. Burkov, *Physical Review B* **96**, 041110 (2017).
- [3] A. Veyrat, K. Koepf, L. Veyrat, G. Shipunov, I. Kovalchuk, S. Aswartham, J. Qu, A. Kumar, M. Ceccardi, F. Caglieris, N. Pérez, R. Giraud, B. Büchner, J. van den Brink, C. Ortix, and J. Dufouleur, *Nature Communications* **16**, 6711 (2025).
- [4] A. Veyrat, V. Labracherie, D. L. Bashlakov, F. Caglieris, J. I. Facio, G. Shipunov, T. Charvin, R. Acharya, Y. Naidyuk, R. Giraud, J. van den Brink, B. Büchner, C. Hess, S. Aswartham, and J. Dufouleur, *Nano Lett.* 10.1021/acs.nanolett.2c04297 (2023).
- [5] D. T. Son and B. Z. Spivak, *Physical Review B - Condensed Matter and Materials Physics* **88**, 1 (2013), arXiv:1206.1627.

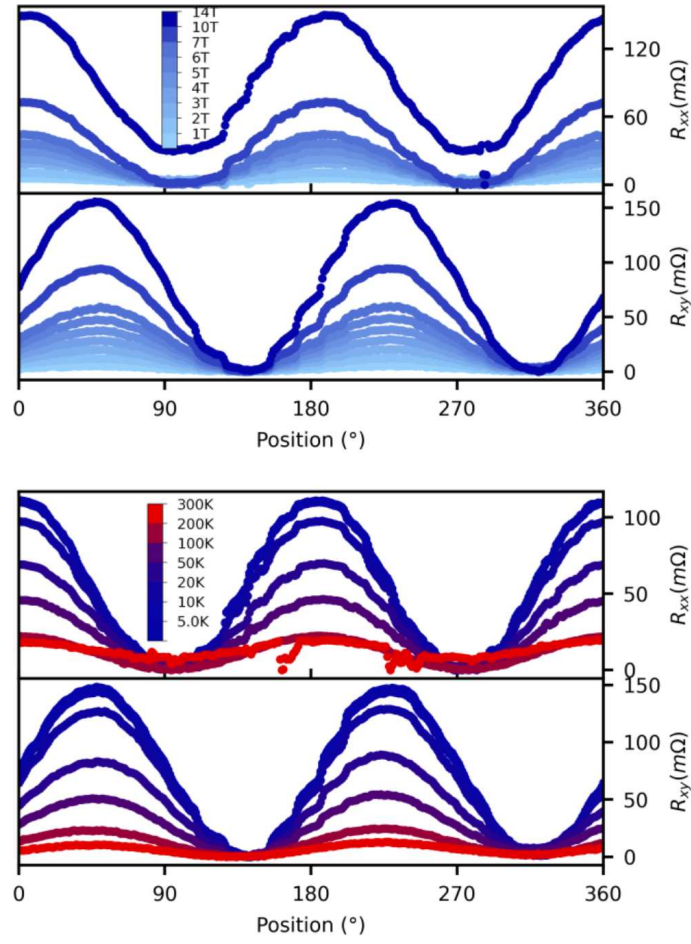


FIG. 5. **a**: Angular dependence of the longitudinal (R_{xx} , top panels) and transverse (R_{yx} , bottom panels) resistances of sample D2 at 5K and multiple fields from 1T to 14T. The plots are shifted vertically for visibility, to share a minimum at 0 Ω . **b**: Same as in **a**, for data taken at 14T and at multiple temperatures from 5K to 300K. The plots are shifted vertically for visibility, to share a minimum at 0 Ω .

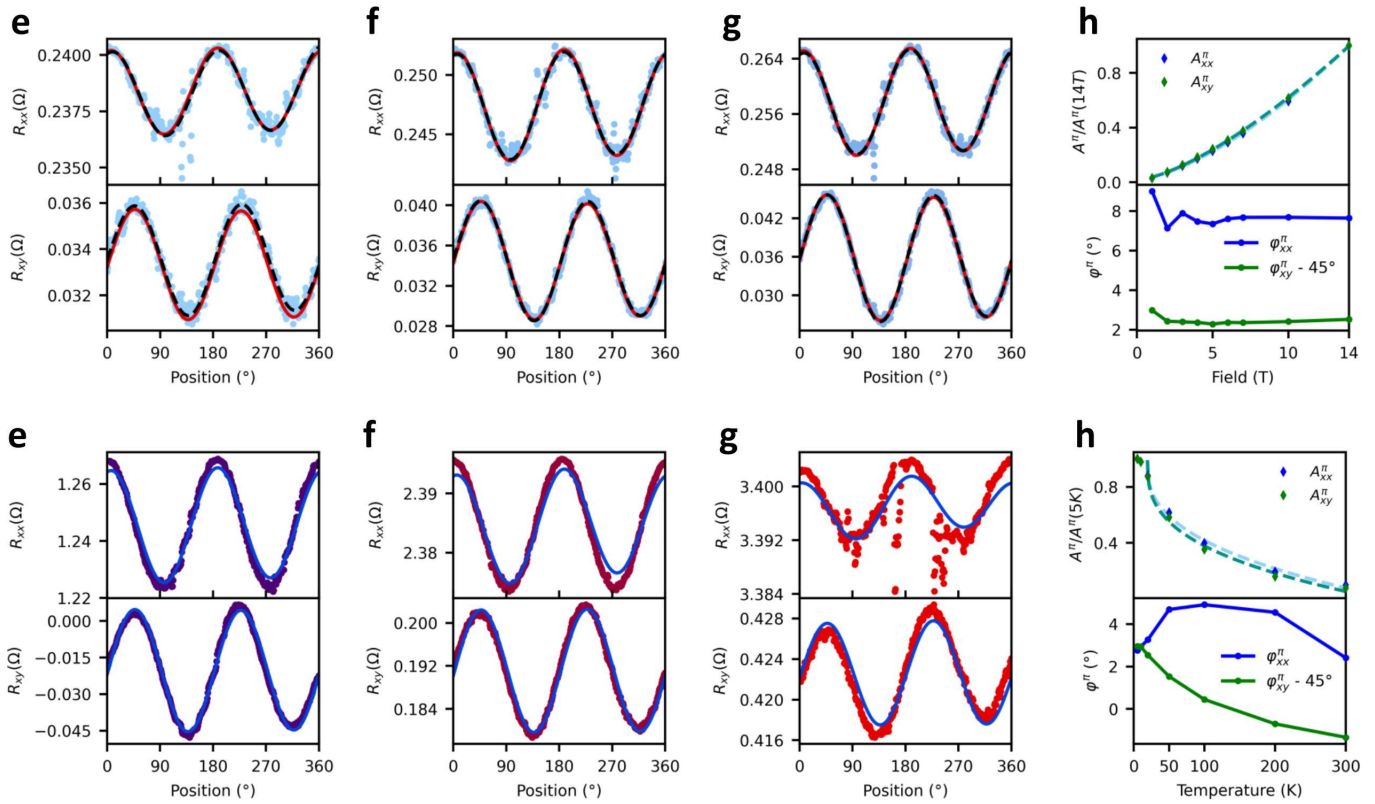


FIG. 6. **a,b,c**: Angular dependence of the longitudinal (R_{xx} , top panels) and transverse (R_{yx} , bottom panels) resistances of sample *D2* at 1.9 K and 1T (a), 2T (b) and 3T (c). as the variation of the phase and the offset are significantly reduced compared to *D1*, the constrained fits of the PHE model (in red) doesn't deviate as much from the measurements at low fields. The data can be fitted very well with an unconstrained π -periodic fit (in dashed black). **d**: Field dependence of the amplitude (top panel, renormalized to its value at 14T) and phase (bottom panel) of the unconstrained fits of the longitudinal (R_{xx} , blue) and transverse (R_{yx} , green) resistances of *D2*. The renormalized amplitudes of the oscillations in R_{xx} and R_{yx} have the same field dependence, as expected for the PHE. The phase does not vary much in field, with an offset of about $45^\circ + 6^\circ$ between φ_{xx}^π and φ_{yx}^π . **e,f,g**: Angular dependence of the longitudinal (R_{xx} , top panels) and transverse (R_{yx} , bottom panels) resistances at 14 T and 100 K (e), 200 K (f) and 300 K (g) for *D2*. The constrained fits of the PHE model (in blue) start deviating from the measurements in R_{xx} at high temperature, as the amplitude of the oscillations are smaller than anticipated from those in R_{yx} , just as in *D1*. The data can still be fitted very well with an unconstrained π -periodic fit (in dashed black). **h**: Temperature dependence of the amplitude (top panel, renormalized to its value at 5 K) and phase (bottom panel) of the unconstrained fits of the longitudinal (R_{xx} , blue) and transverse (R_{yx} , green) resistances for *D2*. The renormalized amplitudes of the oscillations in R_{xx} and R_{yx} have a different dependence in temperature, as the amplitude in R_{xx} decreases more slowly than that in R_{yx} . The phase of the oscillations changes slightly with the temperature.

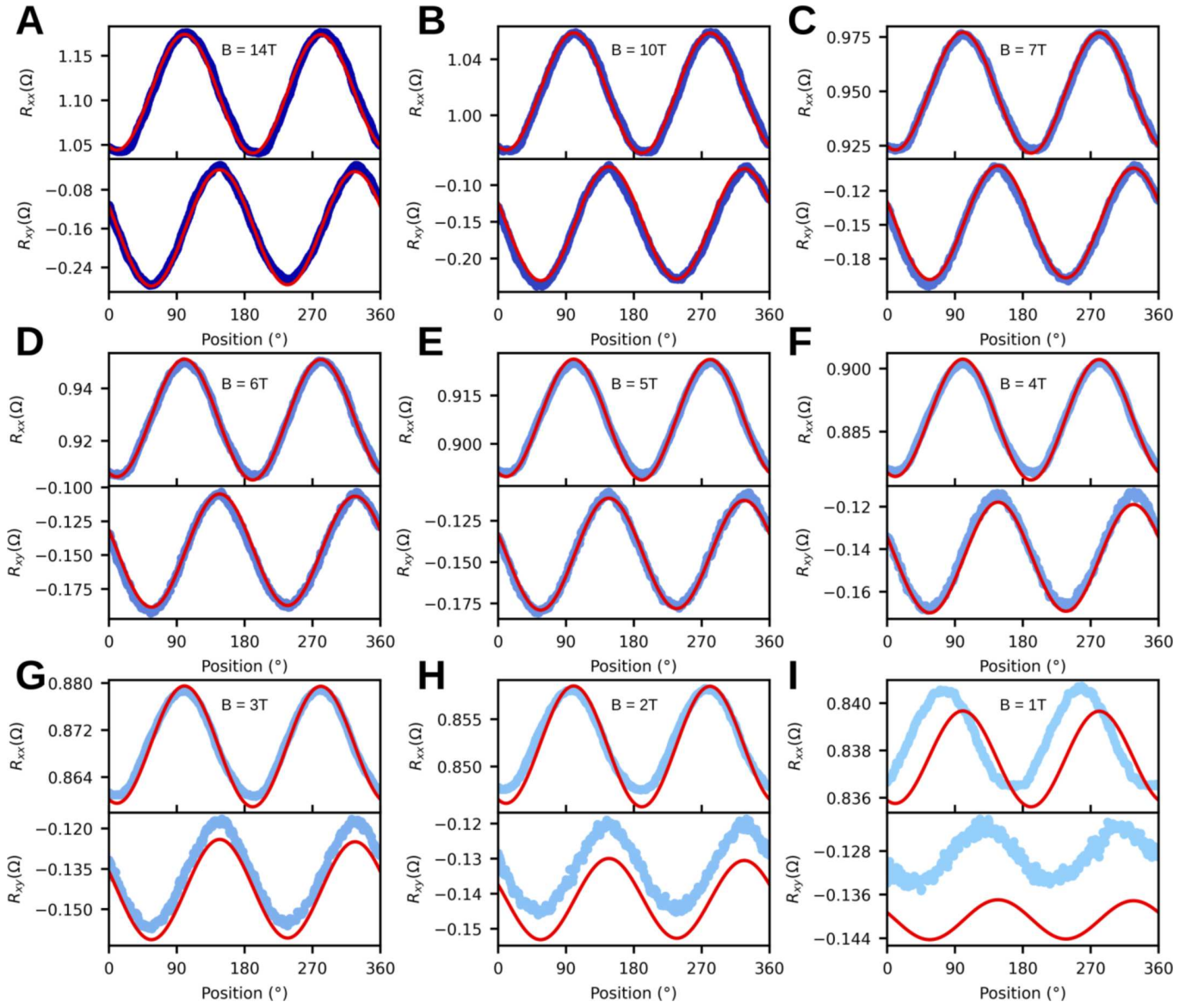


FIG. 7. Raw data: angular dependence of the resistance at different magnetic fields from 1T to 14T for sample D1, at $T=5\text{K}$. The red lines show the fits to the PHE model.

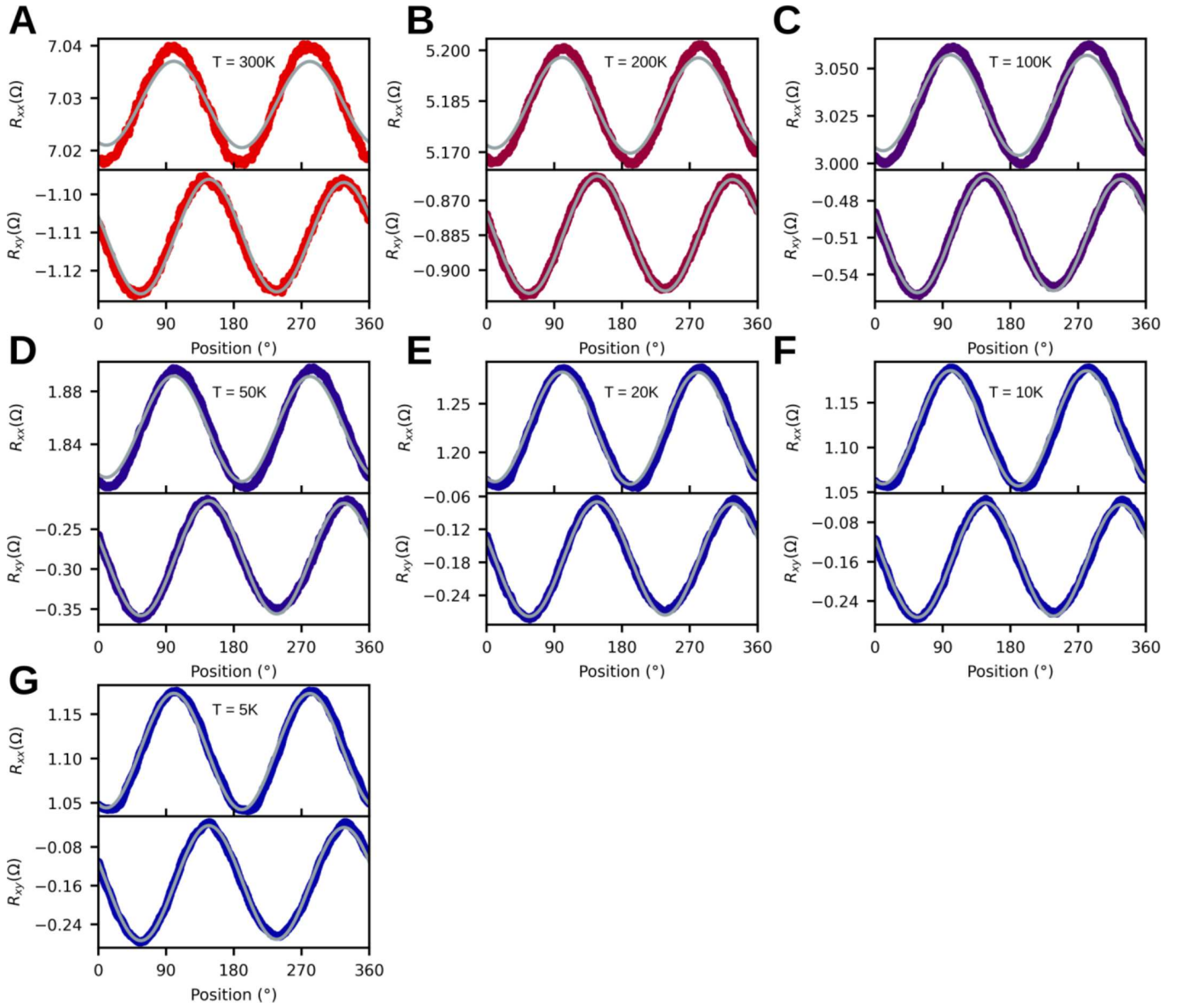


FIG. 8. Raw data: angular dependence of the resistance at different temperatures from 5K to 300K for sample D1, at $B=14T$. The grey lines show the fits to the PHE model.

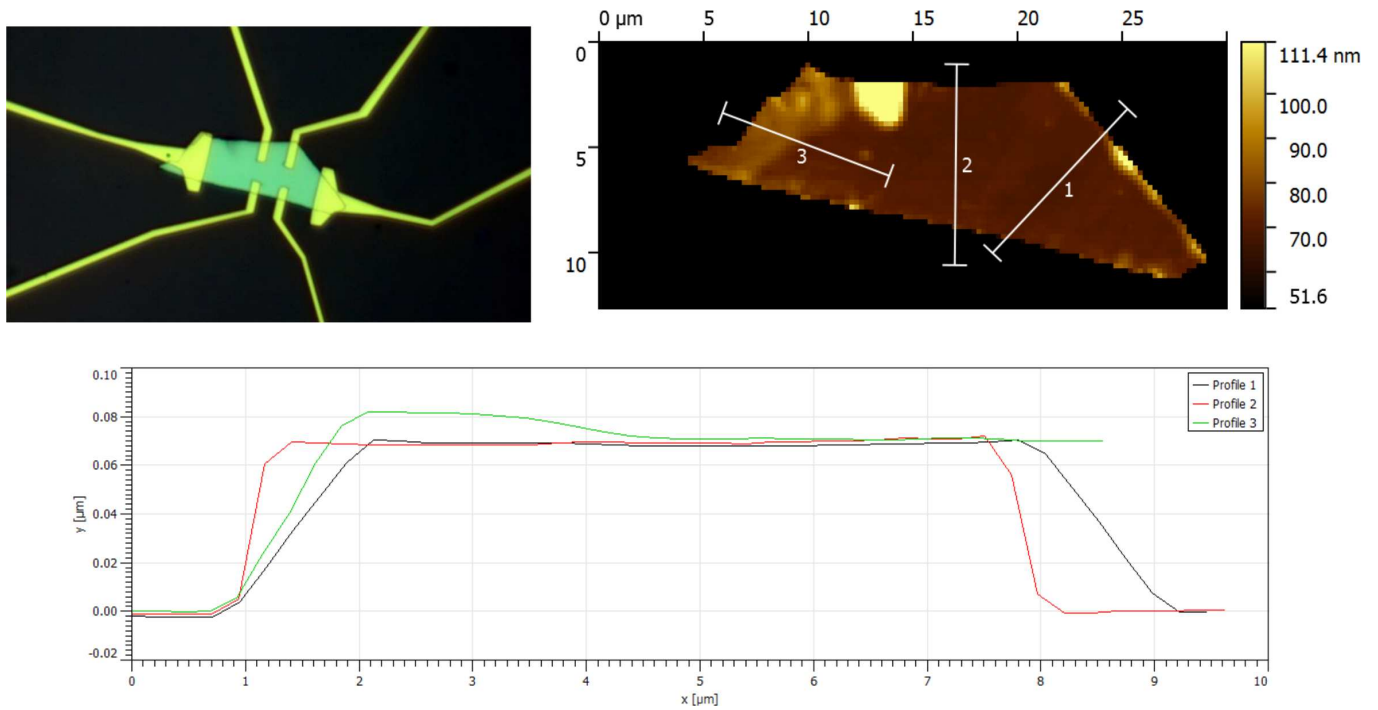


FIG. 9. Optical picture (top left), AFM image (top right) and corresponding profile cuts (bottom) for sample *D1*. The saturated yellow patch probably corresponds to glue residue under (top left) or above (right side) the sample. The flake is shown to be flat over most of its surface, in between the current leads.

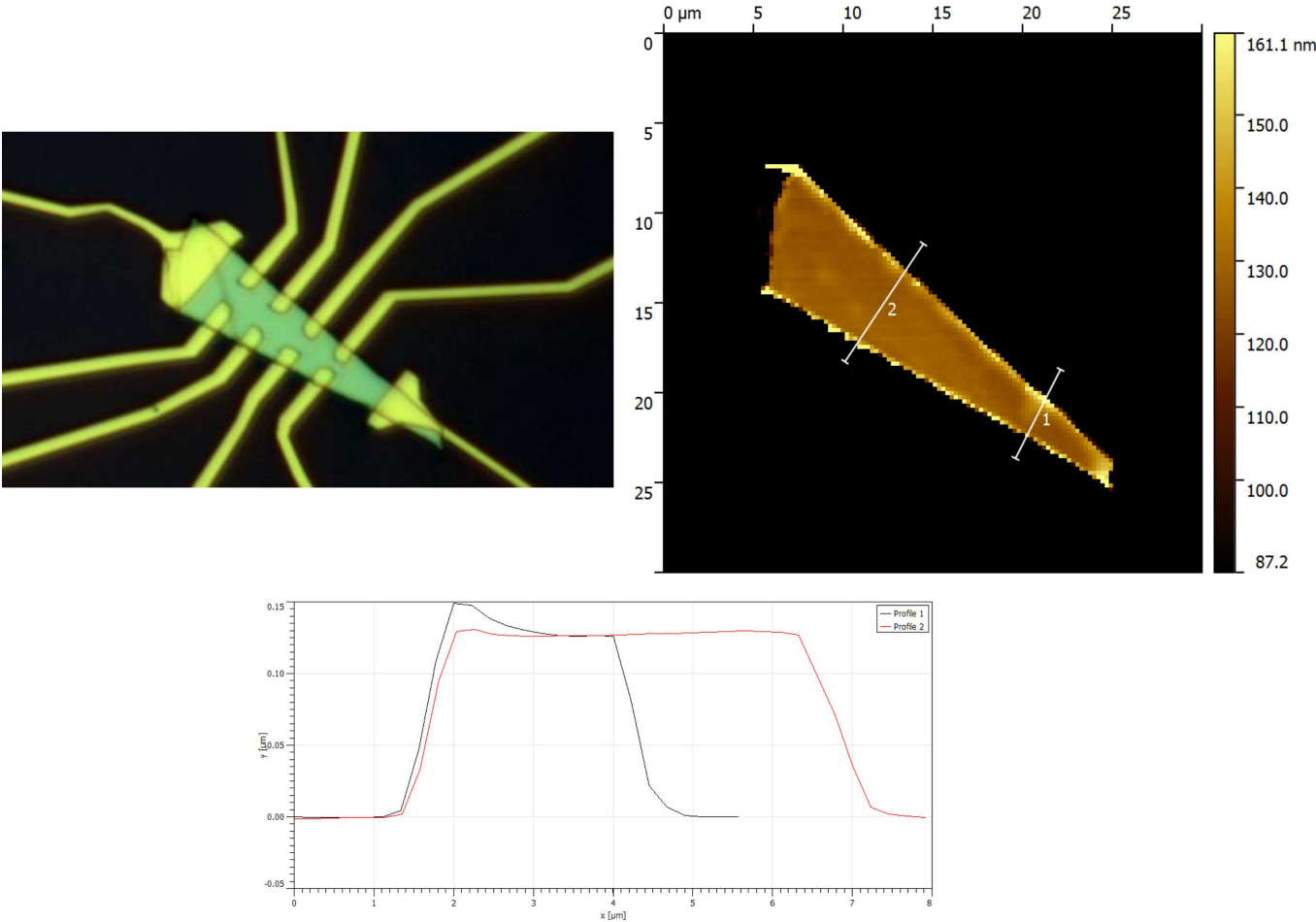


FIG. 10. Optical picture (top left), AFM image (top right) and corresponding profile cuts (bottom) for sample *D2*. The saturated yellow patches probably correspond to glue residue on the edges of the sample. The flake is shown to be flat over most of its surface, in between the current leads.

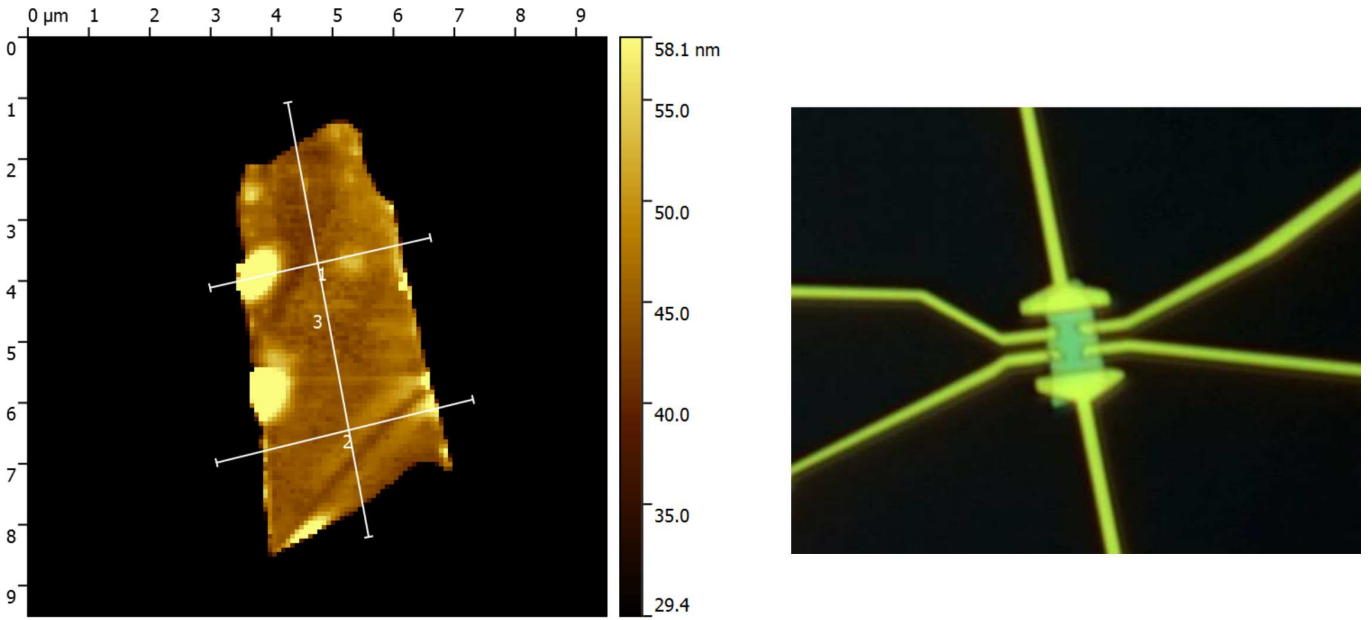


FIG. 11. Optical picture (top left), AFM image (top right) and corresponding profile cuts (bottom) for sample *D4*. The saturated yellow patch probably corresponds to glue residue under (left side) or above the sample. The flake is shown to be flat over most of its surface, in between the current leads.

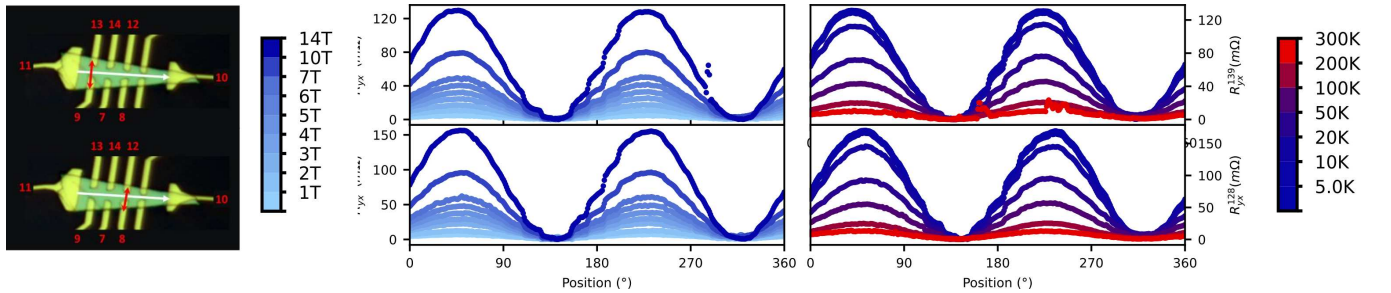


FIG. 12. Transverse resistance measured on sample *D2* for different contact configurations (shown on the left side, with current direction in white and transverse contacts shown in red). The graphs on the left show the transverse resistance at different fields between 1T and 14T at 1.9K, while the graphs on the right side show the transverse resistance at different temperatures between 5K and 300K at 14T. The color scales are shown on the left side (for the fields) and right side (for the temperatures), respectively.

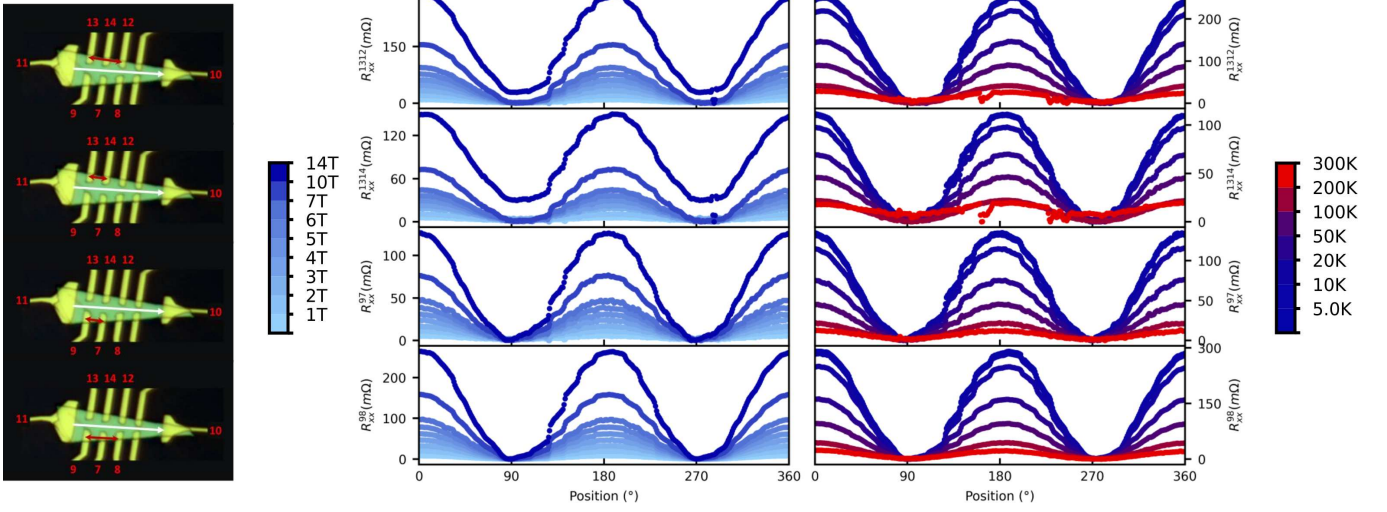


FIG. 13. Longitudinal resistance measured on sample *D2* for different contact configurations (shown on the left side, with current direction in white and Longitudinal contacts shown in purple). The graphs on the left show the Longitudinal resistance at different fields between 1T and 14T at 1.9K, while the graphs on the right side show the Longitudinal resistance at different temperatures between 5K and 300K at 14T. The color scales are shown on the left side (for the fields) and right side (for the temperatures), respectively.

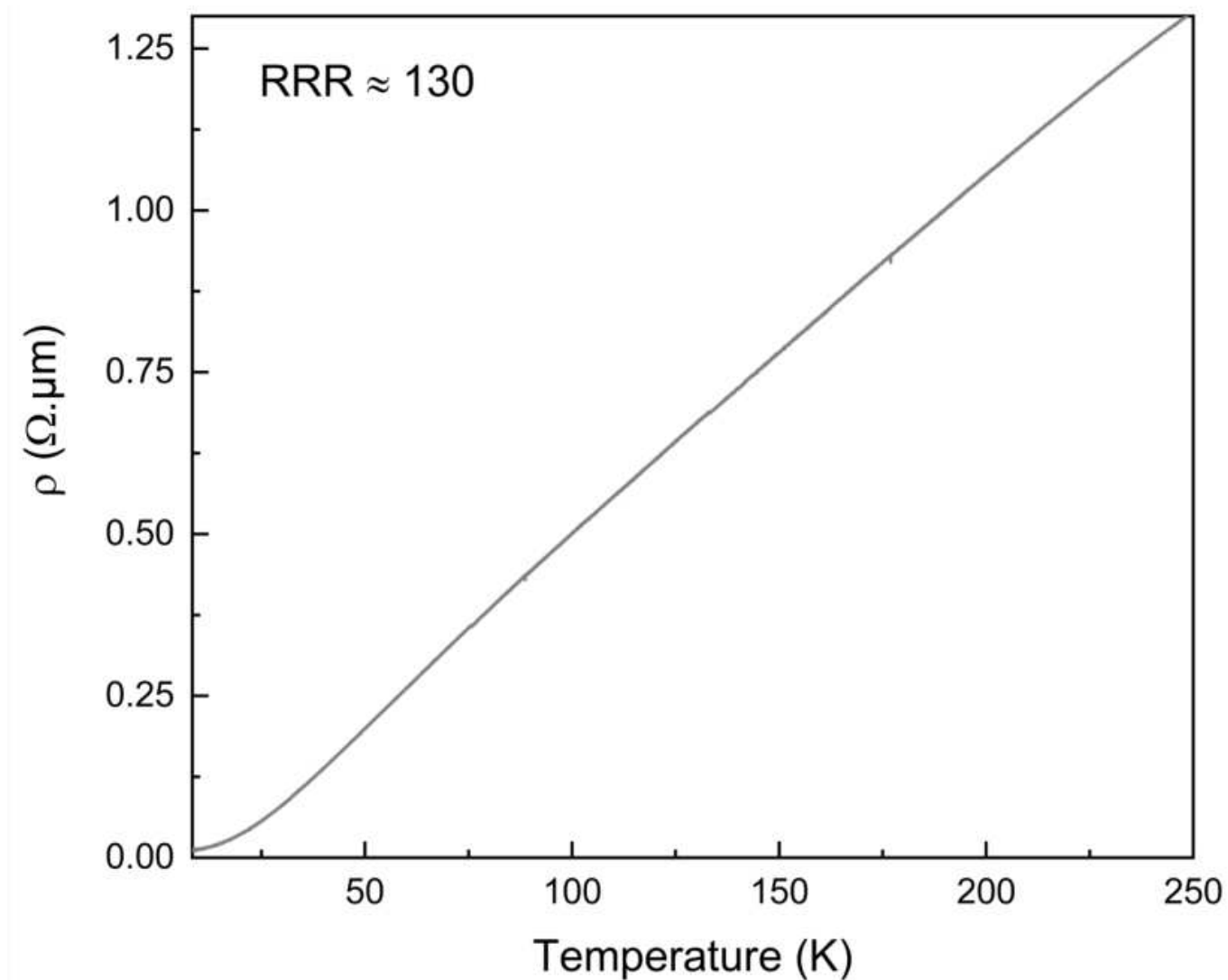


FIG. 14. Temperature dependence of the resistivity of a macroscopic crystal between $T = 300$ K and $T = 4.2$ K. Reprinted with permission from Veyrat et al. *Nano Lett.* 2023, 23, 4, 1229–1235. Copyright 2025 American Chemical Society.

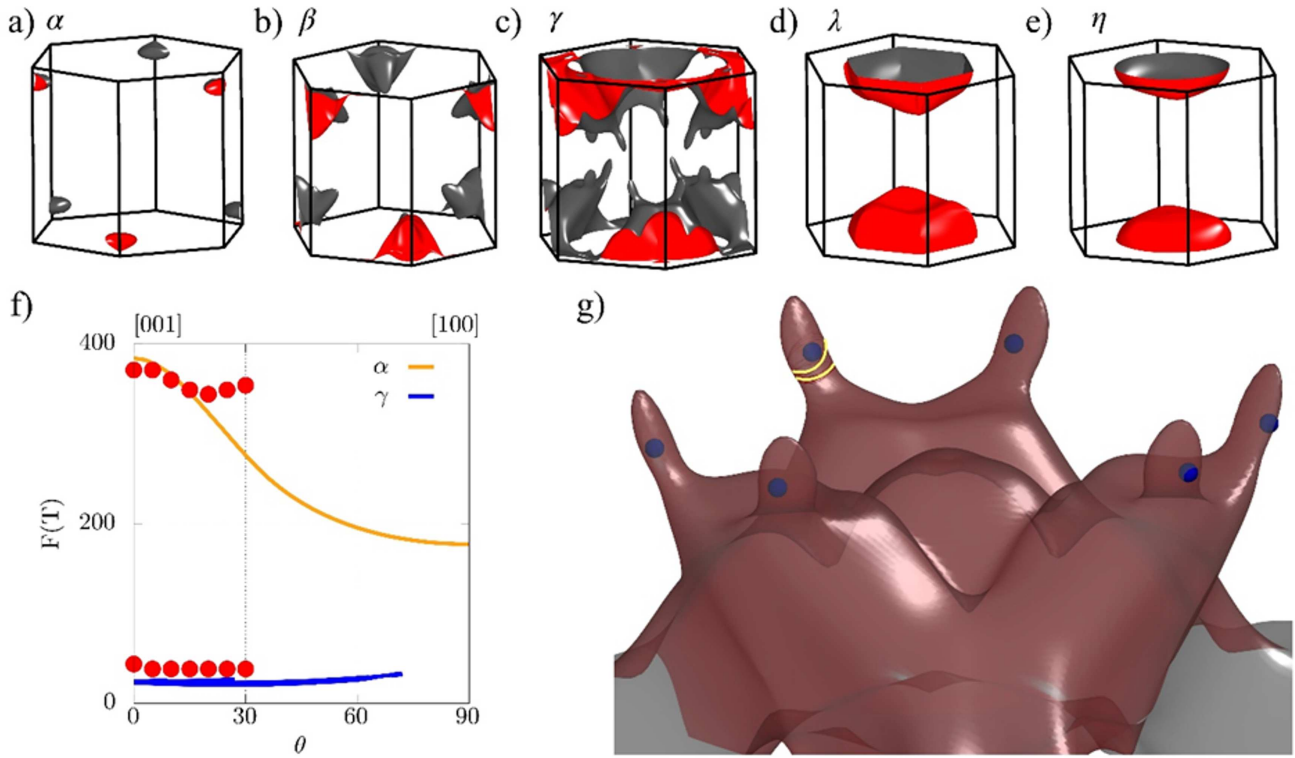


FIG. 15. (a-e) Fermi surface as obtained from density-functional calculations. The outer (inner) face is colored gray (red). (f) Computed quantum-oscillations spectrum at low frequencies. Red points correspond to our experimental results. (g) Extended view of the Fermi surface γ . Weyl nodes are shown as blue points and characteristic extremal orbits of the lowest frequency branch as yellow curves. **Reprinted with permission from Veyrat et al. Nano Lett. 2023, 23, 4, 1229–1235. Copyright 2025 American Chemical Society.**

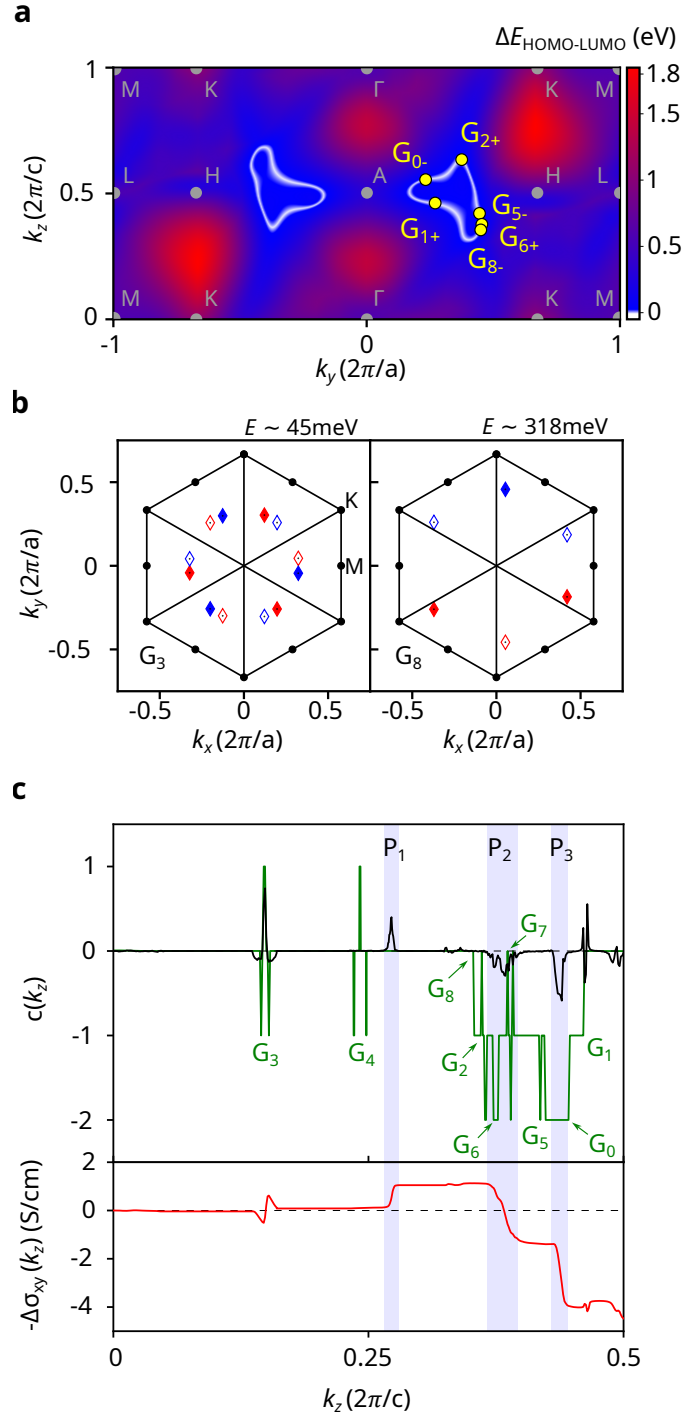


FIG. 16. **Nodal lines and the origin of the anomalous Planar Hall effect in PtBi₂.** **a:** Energy gap ΔE between HOMO and LUMO bands in the k_y, k_z (mirror) plane. The nodal loops ($\Delta E = 0$) appear in white. When $B \neq 0$, each nodal loop splits into 6 Weyl nodes (WN, yellow points), forming 6 groups of 6-WN. The signs denote the chiralities. **b:** Two groups of WN of HOMO-LUMO for a Zeeman energy $E_Z = 14$ meV: G_3 is the 12-fold set of WNs closest to E_F already present at $B = 0$, and G_8 is one of the six 6-fold groups mentioned above. The average energies of the groups are shown. Red (blue) markers denotes positive (negative) chirality, while full (empty) markers denote the positive (negative) k_z position of the WN ($G_3 : k_z \sim \pm 0.149$, $G_8 : k_z \sim \pm 0.358$). Solid lines represent the mirror planes, while the dots show the high-symmetry points. **c:** (Top) Chern number $c(k_z)$ in an ideal (green, full HOMO) and a more realistic (black, $E_F = E_{G_3} = 45.3$ meV) case, with a Zeeman energy $E_Z = 14$ meV. In the ideal case, the Chern number jumps discretely by ± 1 at each WN, while the variation is smoothed out in the realistic case. (Bottom) Anomalous Hall conductivity $-\Delta\sigma_{xy}(k_z)$ calculated from the Chern signal in the realistic case (in black above). The 12 WNs from G_3 at low k_z contribute very little to the AHC, as the Berry curvature they generate is nearly compensated. Most of the AHC comes from 2 peaks in the Chern number at higher k_z , P_2 and P_3 (shown in blue). A third peak at lower k_z , P_1 , attenuates the total AHC amplitude, and is found to correspond to WNs from nodal lines below the HOMO band (see Supplementary materials sec. K). Only the $k_z > 0$ dependences are shown, as $c(k_z)$ is even and $\Delta\sigma_{xy}$ is odd in k_z . **Reprinted with permission from Veyrat et al. Nat Commun 16, 6711 (2025).**

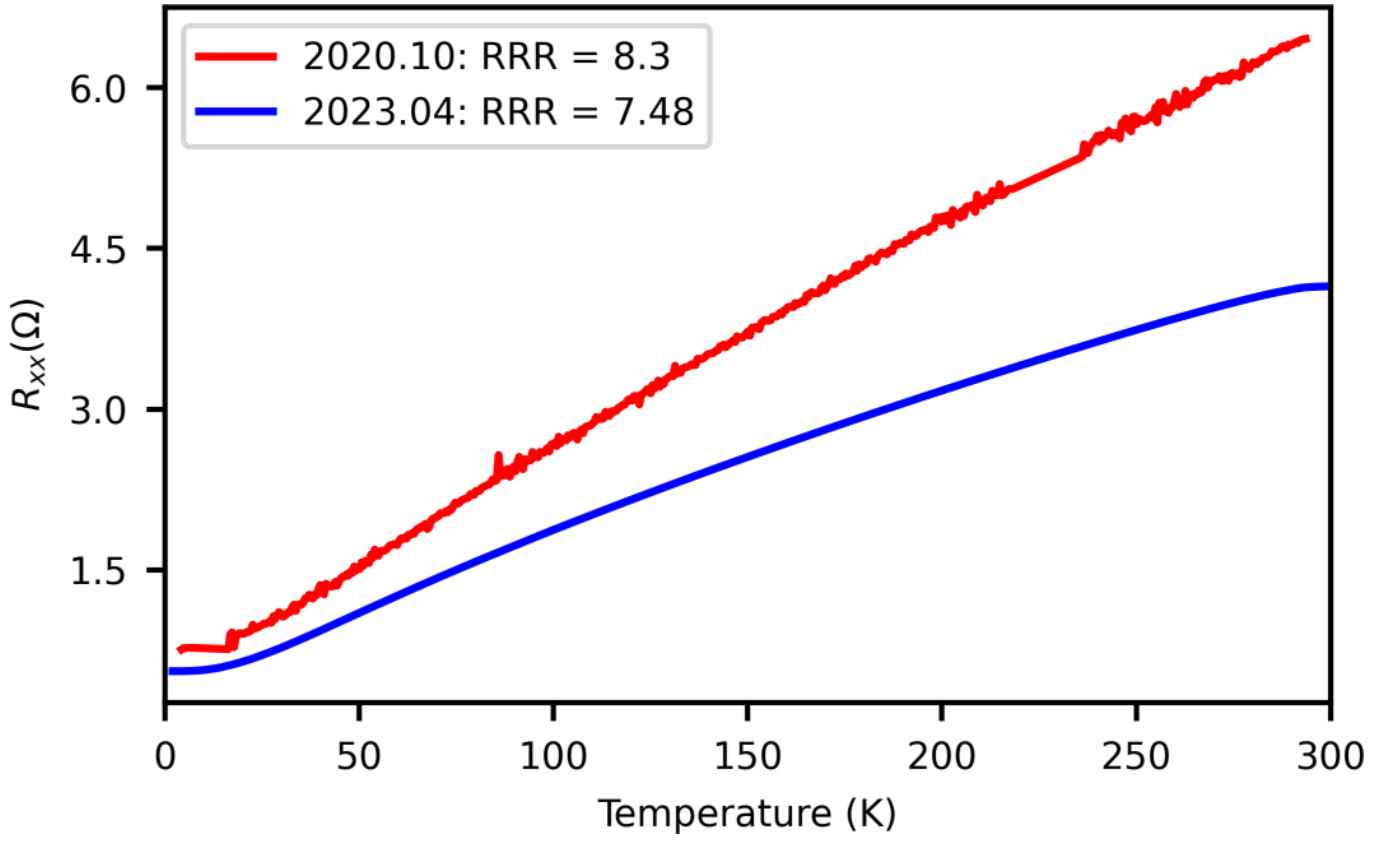


FIG. 17. Comparison of the longitudinal resistance of sample *D1* between two cooldowns from room temperature to 5K. The residual resistance ratio $RRR = \frac{R(300K)}{R(5K)}$ is indicated in the inset. **Reprinted with permission from Veyrat et al. Nat Commun 16, 6711 (2025).**